

A study of the velocity and temperature
boundary layers over a heated rotating disk

Alex Cederholm & Fredrik Lundell

Abstract

In the present work the velocity and temperature boundary layers over a heated rotating disk have been studied. For this purpose a rotating-disk apparatus with a possibility to heat the disk by radiation towards the bottom surface has been built. The temperature distribution of the air above the disk has been measured with constant current anemometry at different radial positions. A thermal video system and liquid crystals were used to measure the temperature on the disk surface. Velocity measurements have been conducted with hot-wire anemometry using a single hot wire oriented in different directions in order to measure two velocity components. The measured velocity and temperature profiles agree well with theory in the laminar region. As the radius is increased, the profiles indicate that Reynolds analogy is valid for this flow if no artificial disturbances are introduced. The disturbance distributions calculated from the measured temperature data do agree with the eigenfunctions obtained from the linear stability analysis. Investigations of the disturbance growth shows that the disturbances are more instationary with heating applied than in the case without heating. The visualizations of the disk temperature with the liquid crystals show that there is a rapid increase of heat transfer close to transition. The liquid crystals also provided a simple way to investigate the influence of different roughness elements on the heat transfer.

Sammanfattning

Temperatur- och hastighetsgränsskikten ovanför en roterande skiva har undersökts. För detta ändamål har en experimentuppställning med en roterande skiva byggts. Skivan värmdes upp medelst lampor som riktades mot skivans undersida. Temperaturen i luften ovanför skivan har mätts med varmtråds anemometri vid olika radiella positioner. Såväl en termisk videoutrustning som flytande kristaller användes för att mäta temperaturen på skivans yta. Hastighetsmätningar utfördes med konstant temperatur anemometri med en enkeltrådsprob som vreds i olika riktningar för att mäta två hastighetskomponenter. De uppmätta hastighets- och temperaturprofilerna överensstämmer väl med teorin i det laminära området. När radien ökas visar profilerna att Reynolds analogi är giltig för strömningen över en roterande skiva om ingen artificiell störning av strömningen görs. Störningsfördelningarna beräknade från temperaturmätningarna överensstämmer väl med den teoretiska förutsägelsen från den linjära stabilitetsanalysen. Genom att studera störningstillväxten har det kunnat konstateras att störningsfältet är mer instationärt när skivan är uppvärmd än i fallet utan uppvärmning. Visualiseringarna av skivans temperatur med flytande kristaller visar att värmetransporten från skivan ökar kraftigt i närheten av den radiella positionen för transition. Med de flytande kristallerna var det också enkelt att studera hur olika störningselement på skivan påverkar värmetransporten från densamma.

Contents

Glossary of symbols	6
1 Introduction	9
1.1 Background	9
1.2 Literature review	11
1.3 Present work	14
2 Theoretical consideration	16
2.1 Laminar base flow	16
2.2 Linear stability analysis	19
3 Experimental apparatus and techniques	26
3.1 The disk apparatus	26
3.2 Instrumentation and techniques	28
4 Results	35
4.1 Velocity and temperature profiles	35
4.2 Disturbance distributions and growth	38
4.3 Liquid crystal visualization	47
5 Discussion	52
5.1 Air velocity and temperature measurements	52
5.2 Liquid crystal visualizations	54
Acknowledgements	56
A Numerical methods	57
B Simple rim lift-up analysis	60
C Single hot-wire multicomponent measurements	63
Bibliography	65

Glossary of symbols

\mathbf{A}_k	matrix [eq.A.6] and [eq.A.1]
\mathbf{B}_k	matrix [eq.A.6]
D	differentiation with respect to z (d/dz)
E	voltage in Kings law [eq.3.1]
E_0	reference voltage in Kings law [eq.3.1]
E_c	compensated value of the anemometer voltage [eq.3.5]
E_m	measured value of the anemometer voltage [eq.3.5]
E_k^i	node component [eq.A.15]
\mathbf{E}	system matrix [eq.A.17]
\mathbf{F}	body force [eq.2.1]
G_k	inhomogeneous righthand side [eq.A.15]
\vec{G}	vector [eq.A.17]
h	the thickness of the aluminium disk (<i>fig.B.1</i>), heat transfer coefficient
\mathbf{I}	the identity matrix
k	summation index [eq.A.6], heat conductivity
k_1	parameter in Kings law [eq.3.1]
k_2	parameter in Kings law [eq.3.1]
l	(<i>fig.B.1</i>)
L	scaling parameter [eq.A.5]
\mathbf{L}	system matrix [eq.A.8]
n	parameter in Kings law [eq.3.1]
N	number of nodes in the computational domain [eq.A.6]
Nu	Nusselt number (hr^*/k)
p	instantaneous non-dimensional pressure field
p^*	instantaneous dimensional pressure field
\bar{p}	non-dimensional pressure disturbance
\bar{p}^*	dimensional pressure disturbance
\tilde{p}	the amplitude of the eigenfunction for pressure disturbance
P	non-dimensional pressure in base flow
P^*	dimensional pressure in base flow
Pr	Prandtl number (ν/σ)
Q	heat transfer rate

r, θ, z	non-dimensional cylindrical coordinates
r^*, θ, z^*	dimensional cylindrical coordinates
r_e^*	the local radius at which the disturbance analysis is conducted
\mathbf{r}	coordinate vector [eq.2.1]
R	nondimensional radius ($r_e^*(\Omega/\nu)^{1/2}$)
Re	Reynolds number (UL/ν)
s	computational node parameter ($s = 1 + L/z_\infty$) [eq.A.5]
St	Stanton number ($Nu/Re/Pr$)
t	non-dimensional time
t^*	dimensional time
T	non-dimensional temperature in base flow ($T(z) = (T^*(z^*) - T_{air}^*)/\Delta T$)
T^*	dimensional temperature in base flow
T_f	temperature of the fluid [eq.3.5]
T_r	reference temperature at calibration [eq.3.5]
T_s	temperature of the hot-wire sensor [eq.3.5]
T_{air}^*	temperature of the ambient air at z_∞
T_{disk}^*	temperature of the heated rotating disk
ΔT	temperature difference between the disk and the air at z_∞ ($T_{disk}^* - T_{air}^*$)
\mathbf{u}	vector notation for velocity [eq.2.1]
u, v, w	instantaneous non-dimensional velocity in the r, θ, z system of coordinates
u^*, v^*, w^*	instantaneous dimensional velocity in the r^*, θ, z^* system of coordinates
$\bar{u}, \bar{v}, \bar{w}$	non-dimensional velocity disturbances in the r, θ, z system of coordinates
$\bar{u}^*, \bar{v}^*, \bar{w}^*$	dimensional velocity disturbances in the r^*, θ, z^* system of coordinates
$\tilde{u}, \tilde{v}, \tilde{w}$	the eigenfunctions for the velocity disturbances
U, V, W	non-dimensional velocity field for base flow in the r, θ, z system of coordinates
U_∞	velocity of the flow (fig.3.3)
U_{meas}	velocity measured by hot wire
U_n	velocity normal to hot wire [eq.C.2]
U_t	velocity tangential to hot wire [eq.C.2]
U_1	velocity measured by hot wire [eq.3.3]
U_2	velocity measured by hot wire [eq.3.3]
y_k	distance between two nodes ($z_k - z_{k-1}$)
z_k	horizontal node value
z_∞	far away boundary in the horizontal direction

α	wave number in the r direction, angle between hot wire and flow direction (<i>fig.3.3</i>)
α_i	imaginary part of the wave number in the r direction
α_r	real part of the wave number in the r direction
$\bar{\alpha}$	$(\alpha - i/R)$ [<i>eq.2.19</i>]
β	wave number in the θ direction
β_i	imaginary part of the wave number in the θ direction
β_r	real part of the wave number in the θ direction
γ	the rim lift-up (<i>fig.B.1</i>)
γ_1	parameter in [<i>eq.2.21</i>]
γ_2	parameter in [<i>eq.2.21</i>]
δ	(<i>fig.B.1</i>)
ζ	non-dimensional axial coordinate inside the disk
$\tilde{\eta}$	eigenfunction for the normal vorticity ($\tilde{\eta} = \alpha\tilde{v} - \beta\tilde{u}$)
κ	the thermal expansion coefficient
λ	$\sqrt{(\alpha^2 + \beta^2)}$ [<i>eq.2.19</i>]
$\bar{\lambda}$	$\sqrt{(\alpha\bar{\alpha} - \beta^2)}$ [<i>eq.2.19</i>]
ρ	density
σ	thermal diffusivity
τ	instantaneous non-dimensional temperature field
$\bar{\tau}$	non-dimensional temperature disturbance
$\tilde{\tau}$	the amplitudes of the eigenfunction for the temperature disturbance
ϕ_i	system parameter [<i>eq.A.1</i>]
$\vec{\phi}_k$	vector of system parameters [<i>eq.A.6</i>]
Φ	vector of vectors of system parameters [<i>eq.A.8</i>]
ν	kinematic viscosity
ψ^k	computational parameter [<i>eq.A.3, A.12, A.13</i>]
ω	disturbance frequency
ω_i	imaginary part of the disturbance frequency
ω_r	real part of the disturbance frequency
Ω	angular velocity
$\mathbf{\Omega}$	angular velocity vector [<i>eq.2.1</i>]

Chapter 1

Introduction

1.1 Background

Heat transfer is an important ingredient in many engineering situations as for instance energy conversion, material processing or cooling of electronic equipment.

When a disk is rotating in still air, the air closest to the disk is driven by friction and rotates with the disk. Since the air is rotating, the centrifugal force gives rise to a radial velocity component. This radial velocity component is zero at the disk surface, since the disk surface is not moving radially, and zero far away from the disk. The radial outflow gives an axial flow downwards, as can be deduced from continuity.

This flow has been studied extensively over the years. In 1921, an exact solution to the Navier-Stokes equations was published by von Kármán. That solution is valid for laminar flow and has been confirmed many times over the years. Flow visualizations have also been made, showing a flow structure with laminar flow near the centre of the disk, outwards spiralling vortices as the radius is increased and further out, transition to turbulence (see figure 1.1). Since these *crossflow vortices* are similar to the ones occurring in the boundary layer over a yawed plate, the rotating disk has been used to model such flows, especially to obtain a better understanding of the transition scenario.

The reason for this resemblance is that in the flow over a plate with a swept edge there exists a pressure gradient in the spanwise direction, driving a velocity component orthogonal to the free-stream comparable with the radial component on the rotating disk.

However, recently an absolute instability for the rotating-disk flow was found theoretically as well as experimentally. Theoretical studies of the swept edge flow show that such flows are not subject to absolute instabilities in the same sense as the disk flow; for this reason, transition studies on the rotating disk may not give total understanding of the transition scenario in swept edge flow.

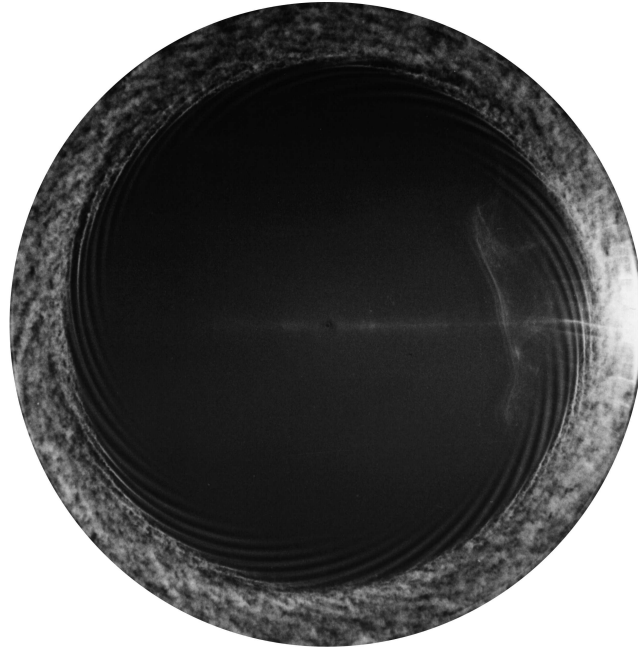


Figure 1.1: Smoke visualization on the rotating disk (Kohama 1978, private communication 1997). From the centre and out, the laminar, vortex and turbulent region are clearly seen.

In the rotating disk case, transition seems to be triggered by disturbances growing at a fixed radial position due to the mentioned absolute instability. On the other hand, in the yawed plate case, transition might be triggered by secondary instabilities growing when the primary disturbances have grown large enough. The growth in the flow over a yawed plate has a convective nature, i.e. the disturbances grow as they follow the flow downstream.

It is important to understand the transition scenario since the properties of a flow drastically change from the laminar to the turbulent region. One of the important features of turbulence is its high rate of mixing that makes a turbulent flow a more efficient transporter of e.g. heat than a laminar flow. In the 19th century the so-called Reynolds analogy between the transport of a passive scalar (like heat in air or salt in water) and momentum was established. It states that the transport of the scalar and the momentum transport (i.e. drag at a surface) is linearly dependent on each other. This is not a universal rule but a rule of thumb. It is well known that the heat transfer predicted by Reynolds analogy can be enhanced by streamwise vortices.

One of the most convenient ways to increase heat transfer with streamwise vortices is to use vortex generators to generate counter-rotating vortices, i.e. two neighbouring vortices that rotate in opposite directions. A vortex generator is any object or disturbance that disturbs the flow enough to generate vortices; it is common to use some kind of obstruction for this purpose. On the rotat-

ing disk the vortices occurring naturally are co-rotating, i.e. all vortices rotate in the same direction. This makes it plausible that an optimal heat transfer enhancing vortex generator for the disk flow should probably be designed in order to generate vortices rotating only in one direction, namely the direction of the naturally occurring vortices.

1.2 Literature review

Flow instability and transition

The Navier-Stokes equations for laminar flow over a rotating disk in still air was solved by von Kármán (1921). Gregory *et al.* (1955) made china-clay visualizations and visualized vortices, stationary to the disk, prior to transition. Numerous experimental investigations on critical and transitional Reynolds numbers have been made, e.g. Kobayashi *et al.* (1980), Kohama (1984) and Wilkinson & Malik (1985). Theoretical linear stability analysis has been performed, e.g. Kobayashi *et al.* (1980) and Malik (1985) giving critical Reynolds numbers and vortex angles in good agreement with experiments. In almost all experiments, transition occurs at Reynolds numbers in close agreement with each other. The non-dimensional radius defined as $r = r^* \sqrt{\Omega/\nu}$ has a value of $513 \pm 3\%$ at the observed position of transition.

In smoke visualizations by Kohama (1984) (see figure 1.1) secondary instabilities of the vortices can be seen. Transition was believed to be triggered by secondary instabilities growing rapidly once the level of the primary disturbance is high enough. Balachandar *et al.* (1992) performed a theoretical analysis of the secondary instability. An important result from their investigation is that there exists a threshold value which the primary type 1 disturbance must exceed, if the secondary disturbance is to be amplified. The threshold value of the root-mean-square of the velocity in the circumferential direction is around 9% of the velocity of the disk surface.

Theoretically, disturbances can only exist for distinct combinations of frequency in time and wavenumbers in the radial and circumferential directions. These distinct combinations can be brought together to different families or branches of solutions to the dispersion relation. The type seen in the visualizations cited above is usually called the type 1 instability.

Faller (1991) presented a theoretical analysis as well as an experimental investigation of a more disturbed flow. He suggested that if the flow is sufficiently disturbed, transition is triggered by the so called type 2 instability, which is unstable for smaller non-dimensional radii but less amplified than the type 1 instability.

Since the structures seen in visualizations are stationary to the disk, most of the work that has been performed has emphasized stationary disturbances. Lingwood (1995) presented an analysis showing that the boundary layer on the rotating disk becomes absolute unstable for travelling disturbances at a non-dimensional radii in good agreement with the experimental transition radii re-

ported by e.g. Kohama (1984) or Wilkinson & Malik (1986). She has also made an experimental investigation (Lingwood 1996) supporting her theoretical results. Her results state that when the non-dimensional radius has a value above 507, disturbances will grow in time for a fixed radial position. This value is in good agreement with the experimental values mentioned above.

The flow becomes absolute unstable due to interaction between travelling disturbances originating from two different types of instabilities, the previous mentioned type 1 together with the heavily damped type 3 instability. The physical interpretation of the absolute instability is that the trailing edge of a wavepacket propagating in the flow has a velocity upstream with the same magnitude as the velocity with which the wave-packet is convected downstream, i.e. the radial position of the trailing edge becomes steady.

The turbulent velocity boundary layer was first studied by von Kármán (1921). In Dorfman (1963) an overview of the work done until then can be found. Later work has been performed by e.g. Cham & Head (1968) and Cebeci & Abbott (1975).

In the present study, measurements were done in the flow over a heated rotating disk. In such a case, buoyancy might effect the flow. In the study by Sreenivasan (1973) it can be seen that buoyancy compresses the tangential velocity and temperature profiles and increases the maximum of the radial and consequently the axial velocities. However, with the parameter values of the present experiment, the effect of buoyancy is very small.

Since the temperature is varying through the boundary layer, so does the viscosity, which is dependent on temperature. Hence, the velocity profiles change when the disk is heated and with them the stability properties. Theoretical studies of such effects have been done by e.g. Kohama & Kobayashi (1980) for a heated curved wall with Görtler instability and Wall & Wilson (1997) for a heated flat plate boundary layer. For a fluid with a viscosity that increases with temperature both these flows seem to be stabilized.

The influence of heating (as well as suction and compressibility) on the stability of the rotating disk boundary layer has been studied by Seddougui & Bassom (1996). Their analysis is restricted to the non-dominant type 2 modes. As before, heating stabilized the flow. Lingwood (1997b) found that suction increases the value of r for the onset of absolute instability in the rotating disk flow (i.e. stabilizes the flow).

Heat transfer and drag

Millsaps & Pohlhausen (1952) presented a similarity solution to the energy equation for the laminar flow over an isothermal heated rotating disk. Later theoretical work has been performed by e.g. Sreenivasan (1973) on the effect of buoyancy as mentioned above and Wang (1990), who studied the case with a concentrated heat source at the centre of the disk.

The total heat transfer has been measured in several investigations from the 50's and forward, e.g. Cobb & Saunders (1953), Richardson & Saunders (1963) and

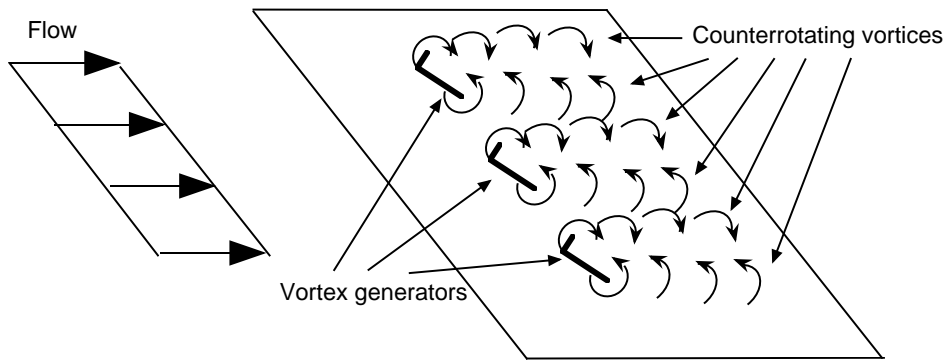


Figure 1.2: Delta wing vortex generators and counter rotating vortices on a flat plate.

Northrop & Owen (1988). Measurements of the local heat transfer have been made by Popiel & Boguslawski (1975) and Elkins & Eaton (1997). The local heat transfer follows the theoretical prediction well in the laminar region. After the laminar region there is a large increase in the transition region and once the flow is fully turbulent, the local heat transfer grows slowly with the nondimensional radius. The local Nusselt number, defined as $hr^*/k = Qr^*/\Delta Tk$, where Q is the heat transfer rate (W/m^2) and k the heat conductivity of air, varies as r and $r^{1.6}$ in the laminar and turbulent region respectively. In the laminar region, where the Nusselt number varies as r , the physical heat transfer is actually constant for an isothermal disk. There exists a similarity solution for the temperature over an isothermal disk for all r and since the temperature difference is constant, so should the heat transfer. In the turbulent region the physical heat transfer increases slowly with r . In the laminar and turbulent region the results by Popiel & Boguslawski (1975) and Elkins & Eaton (1997) agree fairly well.

In the transition region between the laminar and the turbulent regions the heat transfer rate increases abruptly. The position for this sharp increase is reported at $r=442-500$ by Popiel & Boguslawski (1975) and at $r=538-600$ by Elkins & Eaton (1997). The discrepancy between the experiments could be due to the smoothness and low disturbance level in the experiments of Elkins & Eaton and the different temperature difference used. The temperature of the disk was much larger in the experiments of Popiel & Boguslawski than in the experiments of Elkins & Eaton; this influences the effective viscosity in the boundary layer. The viscosity used to establish relationships between the heat transfer and the non-dimensional radius was in both cases calculated from the viscosity of the ambient air far away from the disk. In addition to this, changing the temperature difference most probably changes the stability properties via the mean velocity profiles as mentioned above.

Matsubara & Alfredsson (1996) and Kohama & Ohta (1995) are examples of experiments where naturally occurring vortices (in a rotating channel resp. over a heated water surface) increase the heat or vapour transfer from a surface. For some parameter combinations in the rotating channel case, the heat transfer

from one of the walls increases without the same increase in drag, i.e. the Reynolds analogy is not valid in that case.

Studies on the use of vortex generators (see figure 1.2) to increase heat transfer is reviewed by Jacobi & Shah (1995). They cite various investigations where the heat transfer has been largely increased with a smaller increase in drag using different vortex generators in channel flows and boundary layers. One important conclusion from their review is that the height of the vortex generator has to be of the same order as the local boundary layer thickness if the heat transfer is to be increased.

Rahman & Fagri (1992) made a numerical investigation of the flow and heat transfer in a thin liquid film on a rotating disk. Their investigation is restricted to laminar flow and was initiated from a need of evaporators in microgravity environments. In this case the centrifugal force on the disk is utilized both for establishing the flow necessary for efficient evaporating and to create the thin liquid film that is to be evaporated. In such an application increase of heat or vapour transport by vortex generators could be very useful.

Drag measurements have been done by e.g. Theodorsen & Regier (1948). They measured the global drag and by differentiation they could calculate the local drag. The drag shows the same characteristics as the heat transfer, i.e. a low drag in the laminar region (linear in radius as the velocity), a fast increase in the transition region and finally the turbulent region, where the drag is increasing a little faster with r than in the laminar region. Later investigations confirm their results, except for the exact position of the transition region.

The heat transfer and drag results show that Reynolds analogy is valid for the rotating-disk flow in the laminar and turbulent regions. However, it is not clear whether the transition seen in drag measurements and the transition seen in heat transfer measurements are positioned at the same radial position, even though they seem to be positioned close to each other.

1.3 Present work

The present work was initiated by Professor Y. Kohama¹. The main idea was to study how the streamwise vortices seen in flow visualizations on the rotating disk effect the heat transfer from the disk to the surrounding air. It is known that streamwise vortices can be utilized to increase the heat transfer without a corresponding increase in drag, i.e. the energy necessary to drive the flow. Such an effect could be important in many applications where a rotating disk is used in warmer or colder air, e.g. in rotating turbomachinery or computer disks.

The work was performed at the Low Turbulence Wind Tunnel Laboratory at the Institute of Fluid Science, Tōhoku University, Sendai, Japan under the supervision of prof. Y. Kohama. It is presented as a diploma thesis at the Royal Institute of Technology, Stockholm.

First, the relevant theoretical analysis is presented in chapter 2. This includes

¹Institute of Fluid Science, Tōhoku University, Sendai, Japan

the laminar temperature and velocity profiles above the disk and a linear stability analysis of that flow.

In chapter 3 the experimental setup and the experimental techniques that have been used are described. Measurements were conducted of air velocity and temperature and the temperature of the disk.

The results are presented in chapter 4 and discussed in chapter 5.

Three appendices are included in the report. The first describes the numerical method used in the stability analysis, the second is on the temperature distribution inside the disk and how the shape of the disk is influenced by the non-homogenous temperature. Finally the third one discusses the use of a single hot wire for multi-component velocity measurements.

Chapter 2

Theoretical consideration

In this chapter, the theoretical analysis that will be compared with the experimental measurements, is considered.

2.1 Laminar base flow

There exist similarity solutions for the laminar base flow above an infinite rotating plane and this problem was first solved by von Kármán (1921). Comparing these similarity solutions with the experimental results can give a first indication of whether the measurements with the available experimental equipment are trustworthy.

The starting point of the analysis is the Navier-Stokes equation in a rotating frame of reference along with the continuity equation given in vector notation; \mathbf{r} is the coordinate vector, $\boldsymbol{\Omega}$ is the angular velocity vector and \mathbf{F} is the body force vector. The dimensional stars will be omitted for simplicity.

$$\frac{\partial \mathbf{u}}{\partial t} + (\mathbf{u} \cdot \nabla) \mathbf{u} + 2\boldsymbol{\Omega} \times \mathbf{u} + \boldsymbol{\Omega} \times (\boldsymbol{\Omega} \times \mathbf{r}) = -\frac{1}{\rho} \nabla p + \nu \nabla^2 \mathbf{u} + \frac{1}{\rho} \mathbf{F} \quad (2.1)$$

$$\nabla \cdot \mathbf{u} = 0 \quad (2.2)$$

The theoretical calculation of the laminar base flow starts by considering an infinite plane with its upper side exposed to air. The ambient air has kinematical viscosity ν and density ρ . The plane is rotating with an angular velocity Ω around its vertical axis. Cylindrical coordinates (r^*, θ, z^*) , fixed to the disk, are introduced.

The disturbance analysis will be conducted locally, and thus a radius r_e^* and a Reynolds number R are defined. The radius r_e^* is the location of the analysis where $r = R$ and the Reynolds number is given by $R = r_e^* (\Omega/\nu)^{1/2}$, which is a non-dimensional radius. The following reference quantities can now be defined:

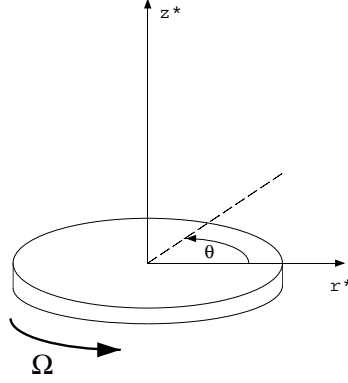


Figure 2.1: The orientation of the cylindrical coordinates (r^*, θ, z^*) and the direction of the angular velocity Ω .

$$\begin{aligned}
 \text{velocity} & \quad r_e^* \Omega \\
 \text{length} & \quad (\nu/\Omega)^{1/2} \\
 \text{pressure} & \quad \rho r_e^{*2} \Omega^2
 \end{aligned} \tag{2.3}$$

The coordinates are non-dimensionalized using the length scale above as follows.

$$\begin{aligned}
 r & = r^* (\Omega/\nu)^{1/2} \\
 z & = z^* (\Omega/\nu)^{1/2}
 \end{aligned} \tag{2.4}$$

The orientation of the axis for the cylindrical coordinates and the origin can be seen in figure 2.1.

With the reference quantities (2.3), it is possible to non-dimensionalize the base flow along with the pressure field (U^*, V^*, W^*, P^*) to the non-dimensional base flow along with the pressure field $(U(z), V(z), W(z), P(z))$. Here $U(z)$, $V(z)$ and $W(z)$ are the velocities in the radial, circumferential and vertical directions respectively. The resulting relations are given below in (2.5).

$$\begin{aligned}
 U^* & = r(\nu\Omega)^{1/2}U(z) \\
 V^* & = r(\nu\Omega)^{1/2}V(z) \\
 W^* & = (\nu\Omega)^{1/2}W(z) \\
 P^* & = \rho\nu\Omega P(z)
 \end{aligned} \tag{2.5}$$

Note that W^* has been non-dimensionalized in a different way compared to U^* and V^* , making W^* independent of the radius. Introducing the definitions

above (2.5) into the Navier-Stokes equation (2.1) and the continuity equation (2.2), the following equations are derived.

$$\begin{aligned}
U^2 - (V + 1)^2 + U'W - U'' &= 0 \\
2U(V + 1) + V'W - V'' &= 0 \\
P' + WW' - W'' &= 0 \\
2U + W' &= 0
\end{aligned} \tag{2.6}$$

The prime denotes differentiation with respect to z .

Since the cylindrical coordinates are fixed to the disk, the boundary conditions imposed at the disk surface ($z = 0$) are that all velocity quantities should be zero. Far away from the disk the velocity quantities should approach the velocity of the air.

$$\begin{aligned}
z = 0 \quad U = 0, \quad V = 0, \quad W = 0 \\
z \rightarrow \infty \quad U \rightarrow 0, \quad V \rightarrow -1
\end{aligned} \tag{2.7}$$

There also exists a similarity solution for the temperature above an infinite rotating heated plane. Following Sparrow & Gregg (1959), we start by introducing the dimensional temperature T^* . The governing equation for temperature is derived from the energy equation.

$$\frac{\partial T}{\partial t} + (\mathbf{u} \cdot \nabla)T = \sigma \nabla^2 T \tag{2.8}$$

The dimensional stars have been omitted for simplicity and σ denotes the thermal diffusivity for the air. With this model we assume constant fluid conductivity, zero internal heat generation, negligible viscous dissipation and negligible compressibility effects.

The temperature of the disk is called T_{disk}^* , the temperature of the ambient air far away from the disk T_{air}^* and the temperature difference between the disk and the ambient air will in the following be denoted $\Delta T^* = T_{disk}^* - T_{air}^*$. With these definitions in mind, the following relation for the non-dimensional temperature $T(z)$ is formed.

$$T(z) = \frac{T^*(z^*) - T_{air}^*}{\Delta T^*} \tag{2.9}$$

The non-dimensional temperature $T(z)$ is introduced into the energy equation (2.8) and the following equation is obtained.

$$T'' = PrWT' \tag{2.10}$$

Here Pr is the Prandtl number defined as $Pr = \nu/\sigma$.

The boundary conditions for $T^*(z^*)$ are $T^*(0) = T_{disk}^*$ and $T^*(z^*) \rightarrow T_{air}^*$ when $z^* \rightarrow \infty$. With (2.9) the boundary conditions are expressed in $T(z)$.

$$\begin{aligned} z = 0 \quad T &= 1 \\ z \rightarrow \infty \quad T &\rightarrow 0 \end{aligned} \tag{2.11}$$

Both the equations for the velocity (2.6) and the equation for temperature (2.10) can be written as a system of first order equations. These systems were solved with a Runge-Kutta method. In order to fulfill the boundary conditions when $z \rightarrow \infty$, a Newton-Raphson iteration for the unknown derivatives at the disk surface, $U'(0)$, $V'(0)$ and $T'(0)$, was used. The boundaries for the computational domain are the disk surface ($z = 0$) and a boundary sufficiently far away from the disk. The result from the computation of $V(z)$, $U(z)$, $W(z)$ and $T(z)$ is shown in figure 2.2.

2.2 Linear stability analysis

Velocity disturbances

The vortices, that can be seen in flow visualizations such as the one shown in figure 1.1, appear when the primary instabilities have grown enough in the radial direction. The following analysis is based on Malik (1985).

An instantaneous dimensional velocity and pressure field (u^* , v^* , w^* , p^*) are defined. Each component consists of a laminar part (U^* , V^* , W^* , P^*) (see section 2.1) and a perturbation part with zero average (\bar{u}^* , \bar{v}^* , \bar{w}^* , \bar{p}^*). The resulting definitions are as follows, using the relations from (2.5).

$$\begin{aligned} u^* &= r(\nu\Omega)^{1/2}U(z) + \bar{u}^* \\ v^* &= r(\nu\Omega)^{1/2}V(z) + \bar{v}^* \\ w^* &= (\nu\Omega)^{1/2}W(z) + \bar{w}^* \\ p^* &= \rho\nu\Omega P(z) + \bar{p}^* \end{aligned} \tag{2.12}$$

With these definitions in mind it is now possible to derive an instantaneous non-dimensional velocity and pressure field (u , v , w , p) by introducing the reference quantities (2.3). The velocities are divided by the reference velocity, $r_e^*\Omega$ and the pressure is divided by the reference pressure, $\rho r_e^{*2}\Omega^2$. The non-dimensional steady part of each component is kept together with a non-dimensional derived quantity. The non-dimensional perturbation quantities are called (\bar{u} , \bar{v} , \bar{w} , \bar{p}).

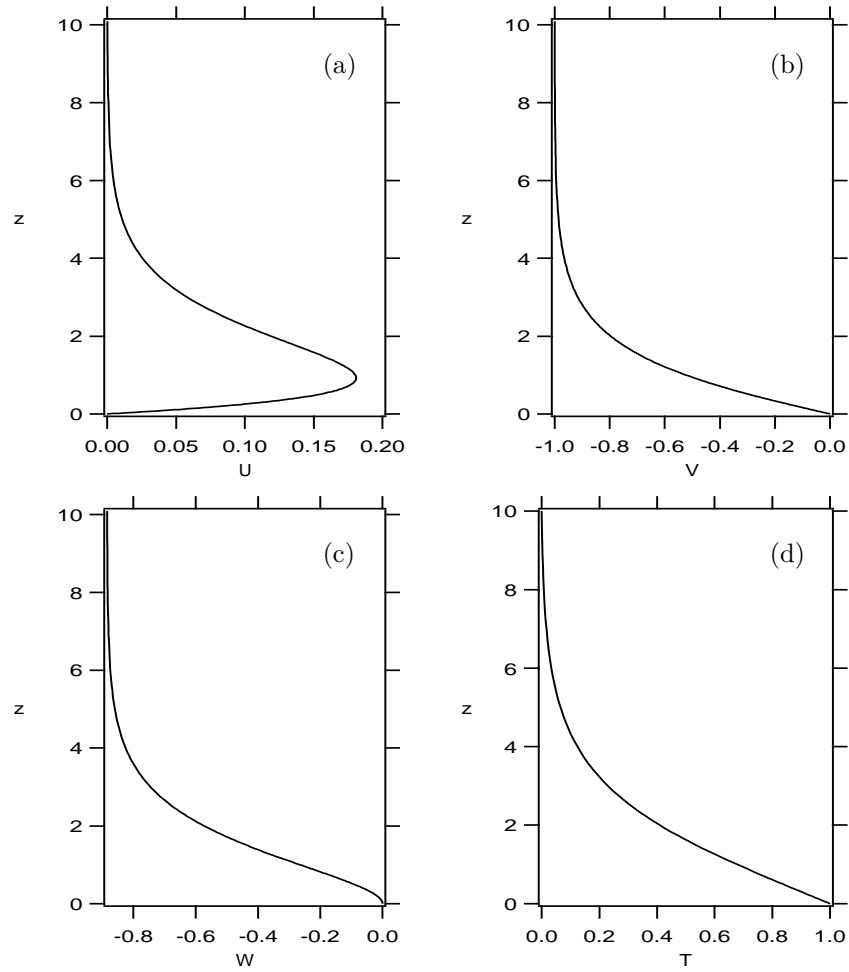


Figure 2.2: Calculated similarity solutions in (a) $U(z)$, in (b) $V(z)$, in (c) $W(z)$ and in (d) $T(z)$.

$$\begin{aligned}
u(r, \theta, z, t) &= \frac{r}{R}U(z) + \bar{u}(r, \theta, z, t) \\
v(r, \theta, z, t) &= \frac{r}{R}V(z) + \bar{v}(r, \theta, z, t) \\
w(r, \theta, z, t) &= \frac{1}{R}W(z) + \bar{w}(r, \theta, z, t) \\
p(r, \theta, z, t) &= \frac{1}{R^2}P(z) + \bar{p}(r, \theta, z, t)
\end{aligned} \tag{2.13}$$

Now the perturbation quantities $(\bar{u}, \bar{v}, \bar{w}, \bar{p})$ are assumed to have the following form.

$$(\bar{u}, \bar{v}, \bar{w}, \bar{p}) = [\tilde{u}(z), \tilde{v}(z), \tilde{w}(z), \tilde{p}(z)] \exp\{i(\alpha r + \beta R\theta - \omega t)\} \tag{2.14}$$

There are two wavenumbers in space, α and β , in the radial and the circumferential direction respectively and one frequency, ω .

By introducing (2.13) and (2.14) into the Navier-Stokes equation (2.1), together with the continuity equation (2.2), and combine, rearrange and linearize with respect to the perturbations, the following four equations are obtained ($\tilde{\eta}$ is the normal vorticity).

$$\alpha\tilde{u} + \beta\tilde{v} + D\tilde{w} = 0 \tag{2.15}$$

$$\tilde{\eta} = \alpha\tilde{v} - \beta\tilde{u} \tag{2.16}$$

$$\begin{aligned}
&[i(D^2 - \lambda^2)(D^2 - \bar{\lambda}^2) + R(\alpha U + \beta V - \omega)(D^2 - \bar{\lambda}^2) - \\
&R(\bar{\alpha}U'' + \beta V'') - iWD(D^2 - \bar{\lambda}^2) - iW'(D^2 - \bar{\lambda}^2) -
\end{aligned} \tag{2.17}$$

$$iUD^2]\tilde{w} + [2(V + 1)D + 2V']\tilde{\eta} = 0$$

$$\begin{aligned}
&[2(V + 1)D - iR(\alpha V' - \beta U')]\tilde{w} + \\
&[i(D^2 - \lambda^2) + R(\alpha U + \beta V - \omega) - iWD - iU]\tilde{\eta} = 0
\end{aligned} \tag{2.18}$$

where

$$D = d/dz$$

$$\bar{\alpha} = \alpha - i/R \tag{2.19}$$

$$\lambda^2 = \alpha^2 + \beta^2$$

$$\bar{\lambda}^2 = \alpha\bar{\alpha} + \beta^2$$

As can be seen $\tilde{\eta}$ is the normal vorticity from which \tilde{u} and \tilde{v} can be calculated. In the derivation of (2.17) and (2.18) the assumption $R \gg 0$ is used, which makes it possible to replace r with R and neglect terms $O(1/R)$ or smaller.

The boundary conditions imposed on these equations are \tilde{w} , \tilde{w}' and $\tilde{\eta} = \alpha\tilde{v} - \beta\tilde{u}$ to vanish at the disk surface ($z = 0$) and when z is approaching infinity they should decay exponentially. The boundary conditions are presented below.

$$\begin{aligned}
z = 0 \quad \quad \quad \tilde{w} = 0, \quad D\tilde{w} = 0, \quad \tilde{\eta} = 0 & \quad (2.20) \\
z \rightarrow \infty \quad D^3\tilde{w} - \gamma_1 D^2\tilde{w} - \bar{\lambda}^2 D\tilde{w} + \gamma_1 \bar{\lambda}^2 \tilde{w} = 0 \\
z \rightarrow \infty \quad D^3\tilde{w} + [\bar{\lambda}^2 - (\gamma_1 + \gamma_2)] D^2\tilde{w} + \\
\quad \quad \quad [\gamma_1 \gamma_2 - \bar{\lambda}(\gamma_1 + \gamma_2)] D\tilde{w} + \bar{\lambda} \gamma_1 \gamma_2 \tilde{w} = 0 \\
z \rightarrow \infty \quad \quad \quad D\tilde{\eta} - \gamma_1 \tilde{\eta} = 0
\end{aligned}$$

where

$$\begin{aligned}
\gamma_1 &= \frac{1}{2}W(\infty) - \left[\left\{\frac{1}{2}W(\infty)\right\}^2 + \lambda^2 - iR(\beta + \omega)\right]^{\frac{1}{2}} \\
\gamma_2 &= \frac{1}{2}W(\infty) + \left[\left\{\frac{1}{2}W(\infty)\right\}^2 + \lambda^2 - iR(\beta + \omega)\right]^{\frac{1}{2}}
\end{aligned} \quad (2.21)$$

The equations (2.17) and (2.18) are separable in r, θ, z, t and together with the boundary conditions (2.20) they constitute an eigenvalue problem for α, β, ω with the two eigenfunctions \tilde{w} and $\tilde{\eta}$.

The numerical method for solving the eigenvalue problem is presented in appendix A.

Having specified R and put $\omega_r = \beta_i = \alpha_i = 0$, the main object is to calculate the modulus of the eigenfunctions. Here the indices r and i stand for the real and the imaginary part respectively. The eigenfunctions are complex, where the eigenfunctions \tilde{u} and \tilde{v} are computed from $\tilde{\eta}$ and the continuity equation.

The starting point is to calculate neutral stability curves, i.e. $\alpha_i = \beta_i = \omega_r = \omega_i = 0$. This is done by iterating with α_r and β_r until $\phi_1(0) = 0$ is fulfilled, as described in appendix A. Setting ω to zero implies neutral disturbances stationary to the disk. In figure 2.3 the neutral stability curve is shown in a (R, α_r) plane and in a (R, β_r) plane respectively.

The neutral stability curve consists of two branches, type 1 instabilities and type 2 instabilities. Inside these branches the solution is unstable with $\omega_i > 0$ and here we find the most amplified solution for a specified R . Outside these branches the solution is stable with $\omega_i < 0$.

The obtained values from the neutral stability curves can be used as starting guesses to calculate the most amplified disturbance. As the disturbance with

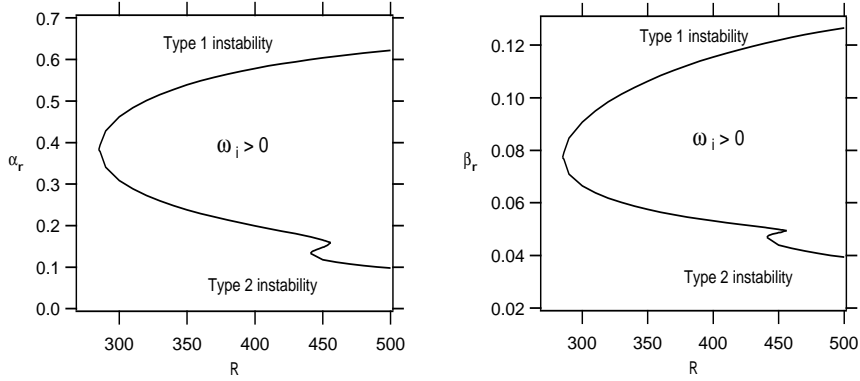


Figure 2.3: Neutral stability curve in a (R, α_r) plane and in a (R, β_r) plane respectively.

the largest amplification is the main concern ω_i has to be maximized. This is done by having good starting guesses for α_r and β_r and then iterate with these until the boundary condition $\phi_1(0) = 0$ is fulfilled again with a ω_i as large as possible.

Case 1 is the most amplified solution for $R = 300$, case 2 and case 3 are neutral solutions to compare with for $R = 400$. In table 2.1 the relevant data is shown for the three different cases used.

case	R	α_r	β_r	ω_i
case 1	300	0.382	0.0774	0.000600
case 2	400	0.578	0.116	0
case 3	400	0.200	0.0532	0

Table 2.1: For all the three cases the following is valid $\alpha_i = \beta_i = \omega_r = 0$

In figure 2.4a the absolute normalized values of \tilde{v} is shown for the three different cases. The three different curves almost coincide and are almost independent of R .

In figure 2.4b the absolute value of the eigenfunctions \tilde{u} , \tilde{v} and \tilde{w} are normalized with the maximum value of \tilde{v} for case 1 is shown. This figure shows the different character of the eigenfunctions and that the eigenfunction of the circumferential velocity \tilde{v} has the largest amplitude.

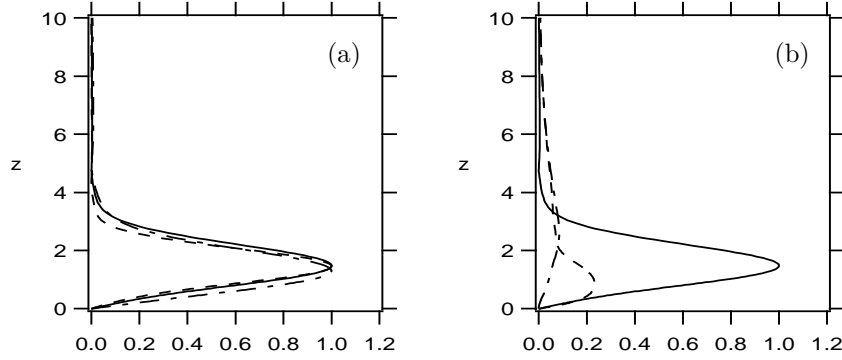


Figure 2.4: In (a) the absolute normalized value of the eigenfunction \tilde{v} for case 1, case 2 and case 3 with respectively solid line, dashed line and dash-dotted line are shown. In (b) absolute values of the eigenfunctions \tilde{u} , \tilde{v} and \tilde{w} normalized with the maximum value of \tilde{v} for case 1 with solid line, dashed line and dash-dotted line respectively, are shown.

Temperature disturbance

Once the wavenumbers and velocity eigenfunctions are known, the temperature disturbance eigenfunction can be calculated.

As with the velocity above, the temperature field is divided into a stationary part, T and a fluctuating part, $\bar{\tau}$. The instantaneous temperature field τ is thus written:

$$\tau = T + \bar{\tau} \quad (2.22)$$

Assuming that $\bar{\tau}$ can be written on the following form,

$$\bar{\tau} = \tilde{\tau}(z) \exp\{i(\alpha r + \beta R\theta - \omega t)\} \quad (2.23)$$

and introducing (2.22) with (2.23) into the nondimensional form of the energy equation (2.8), the following ordinary differential equation for $\tilde{\tau}$ can be derived:

$$[D^2 - PrWD + iRPr(\omega - \alpha U - \beta V) - \lambda^2] \tilde{\tau} = RPrT' \tilde{w} \quad (2.24)$$

where we remember the definitions from (2.19) and prime denotes differentiation with respect to z . The boundary conditions are:

$$\begin{aligned} z = 0 & \quad \tilde{\tau} = 0 \\ z \rightarrow \infty & \quad \tilde{\tau} \rightarrow 0 \end{aligned} \quad (2.25)$$

Equation (2.24) was solved with a second order finite difference scheme for α , β , ω and \tilde{w} obtained from the velocity disturbance calculation. In order to fulfill the boundary condition as $z \rightarrow \infty$, the numerical solution was put equal to the damped mode of the equation that is obtained when $z \rightarrow \infty$ in (2.24) for the far away boundary of the computational domain. The amplitude of the eigenfunction for the most unstable eigenmode for $R=300$ is shown in figure 2.5.

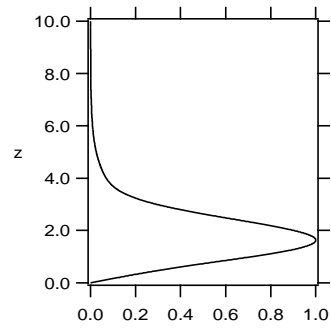


Figure 2.5: Amplitude of the temperature disturbance eigenfunction $\tilde{\tau}$ for the most unstable stationary eigenmode at $R=300$: $\alpha_r = 0.382$, $\beta_r = 0.0774$ and $\omega_i = 0.000600$.

Chapter 3

Experimental apparatus and techniques

3.1 The disk apparatus

The experimental apparatus is shown in figure 3.1. The rotating disk used in the present study was made of aluminium; it was 19 mm thick and had a diameter of 400 mm. The flatness of the disk was measured with a measuring gauge fitted to the traverse system and was found to be $\pm 10 \mu\text{m}$ when the disk was painted. The disk was mounted horizontally on a hollow stainless steel shaft in a steel frame which was bolted to the floor. An AC-motor was used to rotate the disk and the rotating speed of the disk could be chosen arbitrarily up to 2000 rpm. Since the vibration level of the apparatus increased slightly at rotating speeds above 1500 rpm, most measurements were made at a rotating speed of approximately 1400 rpm. At this rotating speed the radius for absolute instability calculated by Lingwood (1997a), $r = 507$, corresponds to a physical radius r^* of 160 mm. The rotating speed was checked with a stroboscope during measurements. During each measured profile, the rotating speed was constant within 0.2%.

With six adjustment screws on the flange connecting the disk to the axis, the angle between the plane of the disk and the axis could be adjusted in order to get them orthogonal. These adjustments were made by letting the disk rotate slowly and watching the probe and its mirror image on the disk with the probe close to the disk ($100 \mu\text{m}$ or closer). The screws were adjusted so that no change of the distance between the probe and its image could be seen during the rotation. Control measurements of the disk showed that this method, although fast and simple, was at least as accurate as other more complicated methods also tried (measuring gauges and laser-based equipment).

Four 500 W heating lamps, mounted symmetrically on the steel frame below the disk, were used for the heating. Since the disk was rotating, this arrangement made it possible to achieve an axial symmetric temperature distribution on the

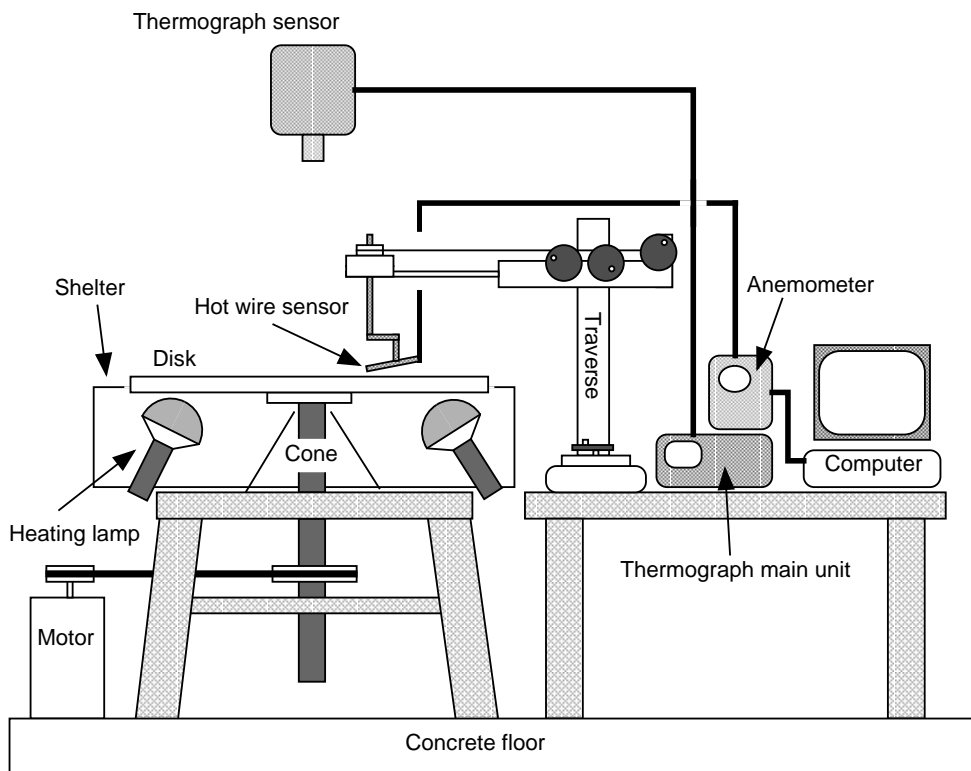


Figure 3.1: Experimental setup

disk. Numerical simulations of the temperature inside, and on the surfaces of, the disk (see appendix B) show that such an arrangement can give a close to isothermal temperature on the upper surface of the disk.

By carefully adjusting the lamps radial position as well as their radiation angles and power, it was possible to get a within ± 1.5 K uniform temperature distribution in the radial direction when the disk temperature was 20 K over ambient temperature. With the thermal video system it could be seen that the axis together with the flange gave rise to an area with higher temperature close to the centre of the disk. This high temperature region was due to heat transferred from the axis, which was heated by the lamps, to the disk via the flange. To get rid of this undesired phenomenon, a cone made of polished aluminium that covered the axis was installed. This cone reflected the radiation that otherwise would heat the axis up towards the bottom side of the disk. With this cone mounted, it was possible to achieve a within ± 0.5 K isothermal temperature on the disk. This was considered sufficiently close to isothermal conditions.

To minimize the influence of the flow from the bottom side of the disk, as well as isolate the heat from the lamps, an aluminium cover over the lamps was built.

It can be expected that the heating arrangement used gives rise to an increased bowl shape of the disk, since the bottom side is warmer and consequently ex-

pands more than the upper side. However, the magnitude of this rim lift-up effect from the heating is smaller than the disks own imperfection, as can be concluded from the simple analysis in appendix B.

3.2 Instrumentation and techniques

Data acquisition and evaluation

All data were sampled with a NEC 9801 computer equipped with a Microscience ADM 1498BPC AD-board. A photo-coupler was used to get a signal with a peak every time the disk passed a fixed position. This arrangement made it possible to fix the signal from the measurement equipment to a frame of reference fixed to the disk. At every measuring point, signals from 30 revolutions of the disk were sampled and saved. The sampling frequency was chosen close to $512\Omega/2\pi$, i.e. one revolution of the disk corresponded to approximately 512 sampling points. The exact number was given by the signal from the photo-coupler.

Before sampling, the signal was amplified and filtered at half the sampling frequency with a DISA 55D26 filter. The raw data was saved on disk for later evaluation on Macintosh computers.

During measurements the signal was observed with an oscilloscope in order to avoid disturbances introduced by other experimental equipment via the power network.

Traverse

A 3D manual traversing system (Mitutoyo CX-652) was used. In order to measure two velocity components with one single wire, the traversing system was equipped with a rotation device that made it possible to rotate the probe in a plane parallel to the disk. The accuracy of the traverse was $10\ \mu\text{m}$ for the translations and 0.5° for the rotation.

All measurements were made with the probe fixed to the laboratory.

To find the vertical position relative to the disk, the probe was observed with a telescope and positioned close to the disk. For a trained eye, "close to the disk" was a constant distance to the disk from day to day. The exact value of this distance was given by the vertical shift needed to get the best possible correspondence between the measured laminar profiles and the theoretical predictions.

Velocity measurements

For most of the velocity measurements reported in chapter 4, the anemometer used was a DISA 55M01 main unit with a 55M10 constant temperature anemometer bridge. The wire used with this bridge was a $2.5\ \mu\text{m}$ diameter,

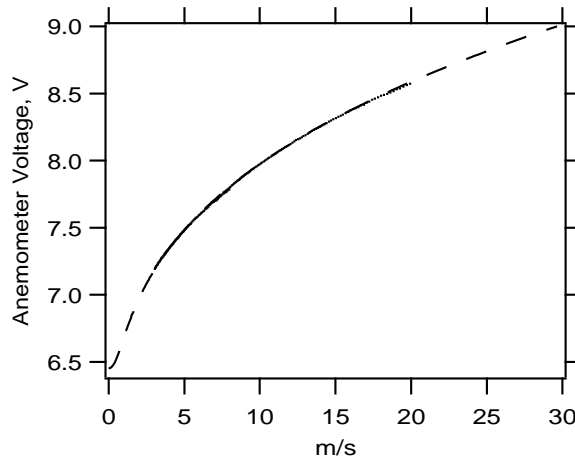


Figure 3.2: Calibration curve for velocity. The dots that resembles a solid line between 3 and 20 m/s are the calibration points, the dashed line is eq. (3.1). Parameter values in this case are $E_0 = 6.45$ V, $n = 0.490$, $k_1 = 0.0149$ V n and $k_2 = 1.61$ V $^{1/2}$.

0.5 mm long platinum wire. The probe with the prongs as well as some simple equipment necessary to solder and etch the wire had to be built. A few of the measurements were conducted with a constant temperature anemometer built by Flow Research Institute in Tokyo together with a 5 μ m diameter, 1 mm long tungsten wire.

When using Constant Temperature Anemometry, CTA, the wire is kept at a constant temperature (higher than the air temperature) by a bridge circuit with a feedback loop keeping the resistance of the wire constant. Since the temperature/resistance of the wire is constant, the convection from the wire to the air is a function of the voltage over the wire, which is measured. The convection is of course increasing as the velocity is increased.

The wires were calibrated with DISA 55D44–46 calibration equipment consisting of a pressure control, a nozzle and a pressure converter. The NEC 9801 computer was used to sample the anemometer signal as well as a signal from the calibration equipment, linear with velocity. This data was later fitted to a modified form of King's law (Johansson & Alfredsson 1982):

$$U = k_1 (E^2 - E_0^2)^{1/n} + k_2 (E - E_0)^{1/2} \quad (3.1)$$

A typical result is shown in figure 3.2. In order to measure two mean velocity components with one single wire (the single wire was preferred for simplicity), the method described below was used. The velocity measured by a hot wire can be expected to vary as

$$U_{meas} = U_\infty \cos \alpha \quad (3.2)$$

where U_{meas} is the velocity measured by the hot wire, U_∞ the velocity of the fluid and α is the angle between the hot wire and the flow direction (see figure 3.3). This relationship can be expected to be valid if α is sufficiently close to zero

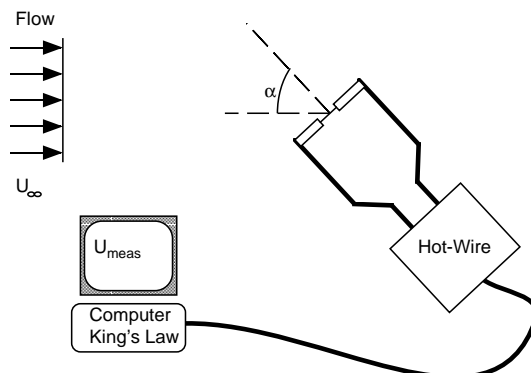


Figure 3.3: Definitions for (3.2)

and the velocity is high enough. For lower velocities and angles differing much from zero, the velocity component parallel with the wire gives deviations from (3.2). From figure 3.4 it can be concluded that (3.2) is a good approximation for $-45^\circ < \alpha < 45^\circ$ for the wires used, if the velocity is high enough.

If the flowfield is expected to be stationary or periodical with a known phase (the latter is the present case), this knowledge makes it possible to measure two velocity components with a single wire by making two measurements at the same position with different angles between the wire and the flow.

Let the two measurements be conducted with an angle difference φ and the flow angle to an arbitrary reference direction be α . For simplicity the direction chosen here is orthogonal to one of the hot-wire directions. With these assumptions the velocity measured in the two measurements can be written as (with indices 1 and 2 referring to the two measurements):

$$U_1 = U_\infty \cos \alpha \tag{3.3}$$

$$U_2 = U_\infty \cos(\alpha - \varphi)$$

from which the flow-angle and velocity can be solved as:

$$\alpha = \arctan \left[\frac{1}{\sin \varphi} \left(\frac{U_2}{U_1} - \cos \varphi \right) \right] \tag{3.4}$$

$$U_\infty = \frac{U_1}{\cos \varphi}$$

This method was used to measure the radial and tangential velocity component. The axial component, which is fairly small, was not taken into account. At large distances from the disk, the axial component is typical 1% of the tangential velocity at the disk (i.e. Ωr^*).

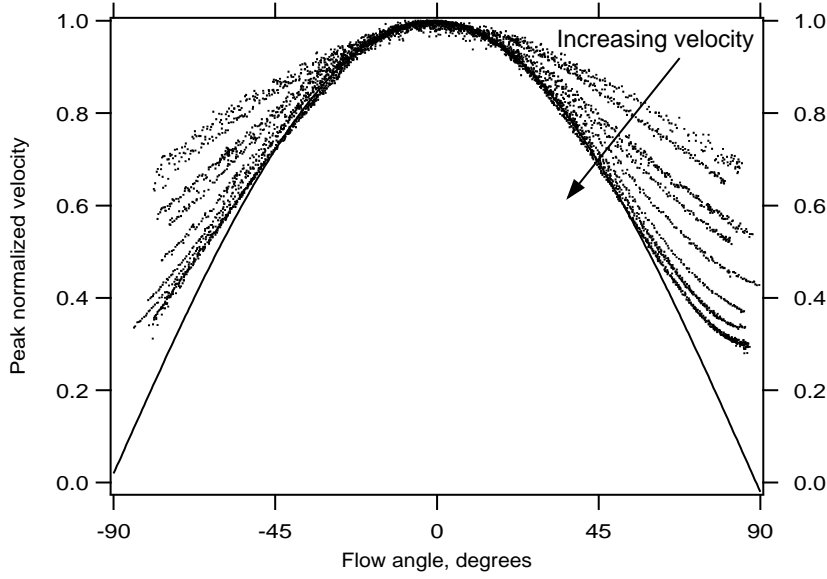


Figure 3.4: Velocities measured by the hot wire as a function of the flow angle for different velocities. The dot-families (most easily distinguished on the right flank) correspond to velocities (from the top and down): 0.9, 1.1, 1.5, 1.9, 2.9, 4.8 and 7.8; the last family is 10, 15 and 20 m/s. The solid line is a cosine slightly shifted to the left for best correspondence to the experimental values.

Of course the deviation from the cosine law (3.2) at "low velocities" gives an error, which increases as the velocity decreases. However, in this case, the velocity is high close to the disk and decreases as the height over the disk is increased. The angle difference φ should be chosen so that $\partial\alpha/\partial(U_2/U_1)$ is small in order to get a small error in α from an error in U_2/U_1 . The derivative is shown in figure 3.5 and as can be seen from that plot, φ should be 90° . But since both α and $\alpha - \varphi$ must be within the range where (3.2) is valid, an intelligent choice of φ has to be made. In the present case, $\varphi = 45^\circ$ was chosen. As can be seen in chapter 4, the method gives good results close to the disk, where the velocity is large, but an increasing deviation from the theoretical prediction with increasing height over the disk is evident.

Quantitative velocity measurements were only performed for the isothermal case and when necessary, the measurements were compensated for drifting room temperature with the formula below, derived in [24]:

$$E_c^2 = E_m^2 \left(1 + \frac{T_f - T_r}{T_s - T_f} \right) \quad (3.5)$$

where E_c is the compensated value of the anemometer tension, E_m is the measured value, and indices f , r and s correspond to the temperature of the fluid, the reference temperature at calibration and the temperature of the hot-wire sensor, respectively. The sensor temperature was calculated from the overheat ratio.

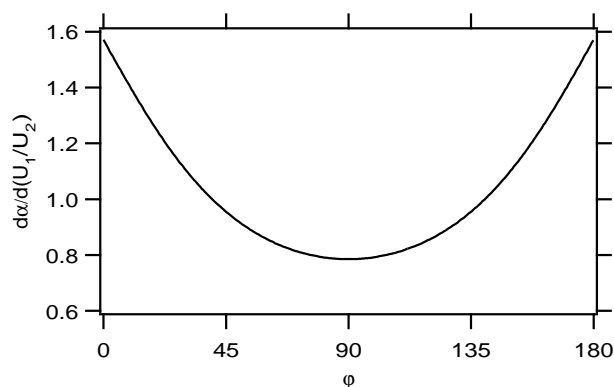


Figure 3.5: The sensitivity for errors in U_1/U_2 on the measurement of α for different φ .

Air temperature measurements

The temperature was measured with Constant Current Anemometry (CCA). The anemometer used was a DISA 5501 main unit together with a 55M20 temperature bridge. The wire used was a $2.5 \mu\text{m}$ diameter, 1 mm long platinum wire. With constant current anemometry a constant current through the wire is used. To measure velocity, the current is chosen so high that the wire is heated to a temperature much higher than the air temperature. The voltage over the wire is then a measure of the heat convection from the wire to the flow (as mentioned earlier this convection is increasing with increasing velocity).

For temperature measurements, the current is chosen so low that the wire is barely heated. Then the voltage over the wire can be measured to give the resistance of the wire, which is linearly dependent of the temperature.

The current through the wire was chosen so that a velocity change from 0 to 20 m/s at a constant temperature gave an error smaller than 1% of ΔT^* in the temperature measurements. When the current had been chosen, the system was calibrated using a Slowly Decreasing Temperature Chamber (SDTC) built for the purpose. The SDTC consisted of a small (0.3 dm^3) isolated box made of styrofoam. The air inside the box was heated to approximately 50°C whereafter the probe was mounted inside the box together with a thermometer. As the air in the box was cooled, calibration data could be obtained.

The calibration data was fitted to a straight line as shown in figure 3.6. The thermometer used for the calibration was later used for the measurements of the ambient temperature far away from the disk during the measurements.

Surface temperature measurements

Two different techniques were used in order to measure the temperature of the disk surface. One was a thermal video system, ALVIO TVS, and the other was

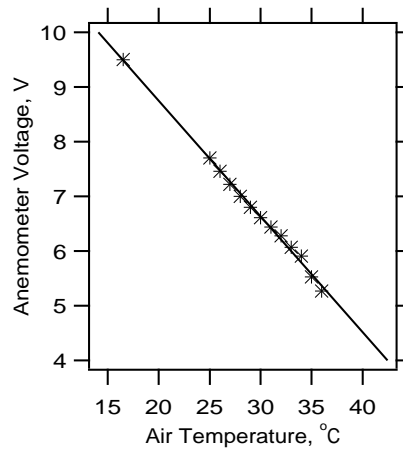


Figure 3.6: Calibration curve for the temperature measurements obtained with the SDTC. The stars are the calibration points, the line is the least square fit to these points, in this case $T = 61.36 - 4.73E$.

liquid crystals.

The liquid crystals used were obtained from Japan Capsule Products Limited. They were delivered as a self adhesive film and could easily be applied to the surface. The range of the sheet used was 33.8–36.8°C with five colours indicating different temperatures in the interval.

To document the liquid crystal visualizations the disk was photographed in stroboscopic light from a Sugawara Digital Strobo S-125. Each flash from this stroboscope lasts 2 μ s and the stroboscope was triggered with the signal from the photocoupler. The camera used was a Nikon F50 camera equipped with a 50 mm lens fitted to the stand also used for the thermograph camera. With ASA 400 film and shutter 1.8, a time of 1/2 second gave a clear exposure.

In order to measure the surface temperature without touching or applying anything to the surface, a thermal video system was used. It uses the spectral information of the radiation emitted from the surface to determine the temperature of a surface; for this reason the disk was painted black. The results from the measurements are presented for the user on a small videoscreen as a picture where it is possible to get the measured temperature at specific points as well as the temperature on the measured area as a contourplot.

The thermal video system was not fast enough to resolve the small structures stationary to the disk that could be visualized with the liquid crystals together with the stroboscopic light. However, the thermal video system could be used to measure the mean temperature for a fixed radius during measurements.

Before measurements, the thermal video system was used to adjust the power and positions of the heating lamps to achieve as an isothermal disk as possible. It was also used to confirm that the rotating speed and the heat conduction inside the disk were high enough to equalize temperature differences that could

occur due to the circumferential non-uniformity of the heating distribution.

The accuracy of the thermal video system was checked by measuring the disk temperature with the thermal video system and the thermometer mentioned above simultaneously. The readings agreed within ± 0.05 K.

Chapter 4

Results

4.1 Velocity and temperature profiles

The measurements reported in this section were, with one exception, made at a rotating speed of 1400 rpm. The exception is the velocity profile at $r=638$, which was measured at a rotating speed of 1800 rpm. The measured profiles are compared with the theoretical prediction from section 4.1 and the deviations from the theoretical profiles give some information about increased drag and heat transfer in the transition region.

All profiles are shown non-dimensionalized as follows:

quantity	non-dimensionalization
length	$\chi = \chi^* \sqrt{\frac{\Omega}{\nu}}$
velocity	$\chi = \frac{\chi^*}{\Omega r^*}$
temperature	$T = \frac{T^* - T_{disk}^*}{\Delta T^*}$

Table 4.1: Non-dimensionalization. The variable χ^* denotes the physical variable to be non-dimensionalized and χ the value after non-dimensionalization.

The velocity profiles were measured with no heating applied. This means that it is necessary to be careful when the velocity and temperature profiles are compared, but still some conclusions about drag and heat transfer can be made.

All points in the profiles are averaged over 30 revolutions of the disk.

Measured velocity profiles for different radii are shown in figure 4.1 together with the theoretical prediction. For the tangential velocity component, the

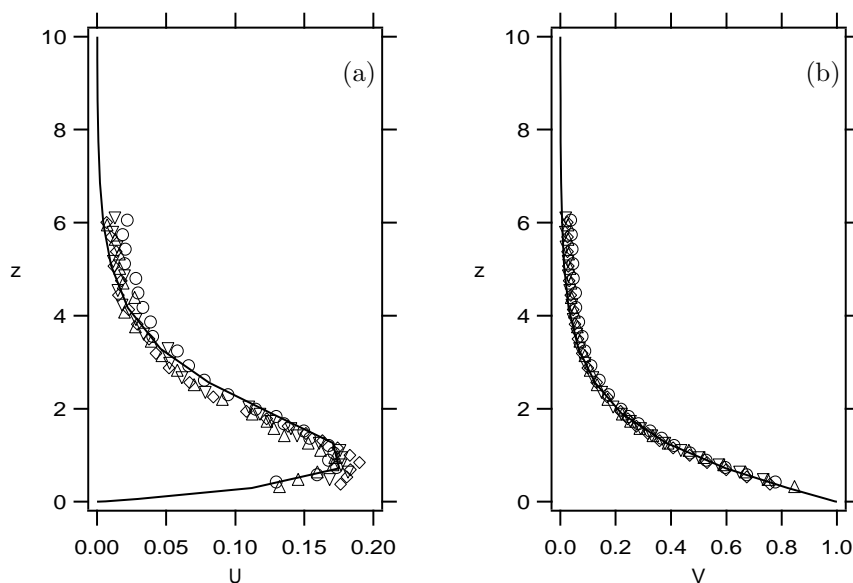


Figure 4.1: Measured radial (a) and tangential (b) velocities at different laminar r , $\circ = 249$, $\triangle = 311$, $\nabla = 374$, $\diamond = 436$. The line is the laminar von Kármán solution.

correspondence between measured data and theory is good close to the disk. Higher up in the boundary layer, there is an increasing deviation from the theoretical prediction, probably due to the axial velocity component but mostly the deviation of the hot-wire sensitivity from the cosine law (3.2) discussed in section 3.2. A relatively larger discrepancy can be seen in the radial component. This is due to the lower velocity; the absolute error can be expected to be approximately equal for the two components.

The measured temperature profiles shown in figure 4.2 also agree with the theoretical curve, even though there is a deviation from the theoretical curve in the upper part of the boundary layer, indicating that there were errors in the method used to measure the ambient temperature far away from the disk. It was measured with the thermometer, previously used for calibration, positioned approximately 0.4 m above the disk. The measured reference value of the ambient temperature seems to be too low.

As the radius is increased, the velocity and temperature profiles deviate from the small-radii ones. In figure 4.3 it can be seen that there is a gradual change in the velocity profile, which is due to transition from laminar to turbulent flow. The velocity profile at $r = 436$ seems to be unaffected and at $r = 561$ the profile is fully turbulent. The same scenario is seen in the temperature profile, see figure 4.4. The temperature profile at $r = 453$ is still laminar, and the profile at $r = 552$ is fully turbulent. Since the velocity and temperature profiles change at approximately the same r , there is no large region with large heat transfer and low drag. All r have been calculated using the same viscosity, namely the viscosity of the ambient air.

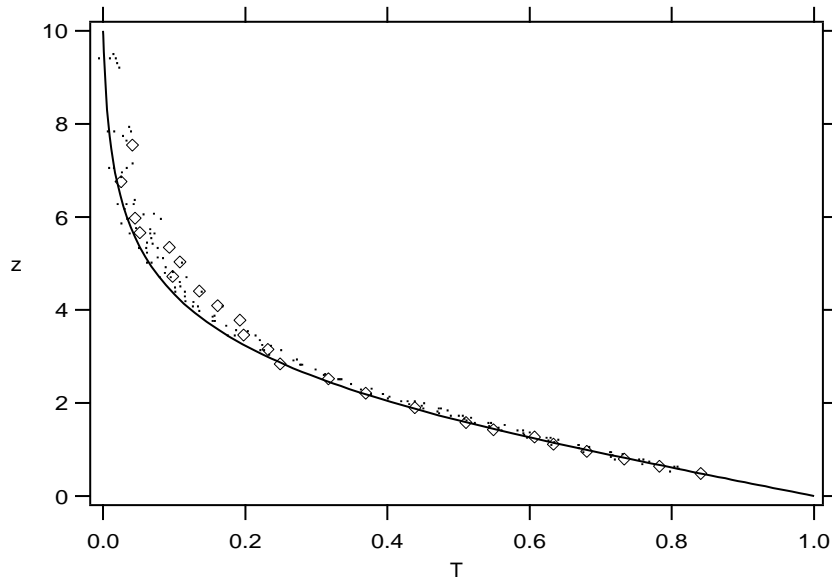


Figure 4.2: Measured temperatures at different r . The dots are from $r = 200$, 250, 299, 352 and 402, whereas the diamonds are $r = 453$. The line is the laminar theoretical solution.

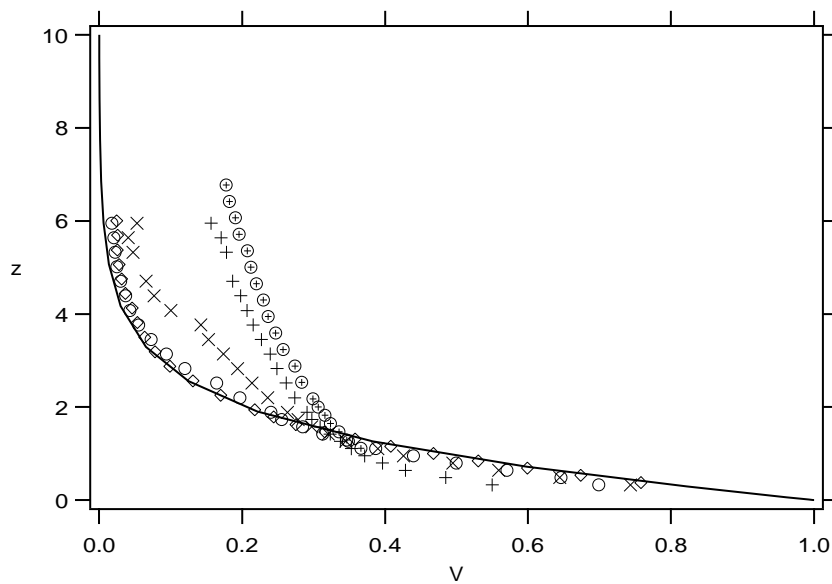


Figure 4.3: Measured radial velocities at different r : $\diamond = 436$, $\circ = 468$, $\times = 499$, $+$ = 561 and $\oplus = 638$. The line is the laminar von Kármán solution.

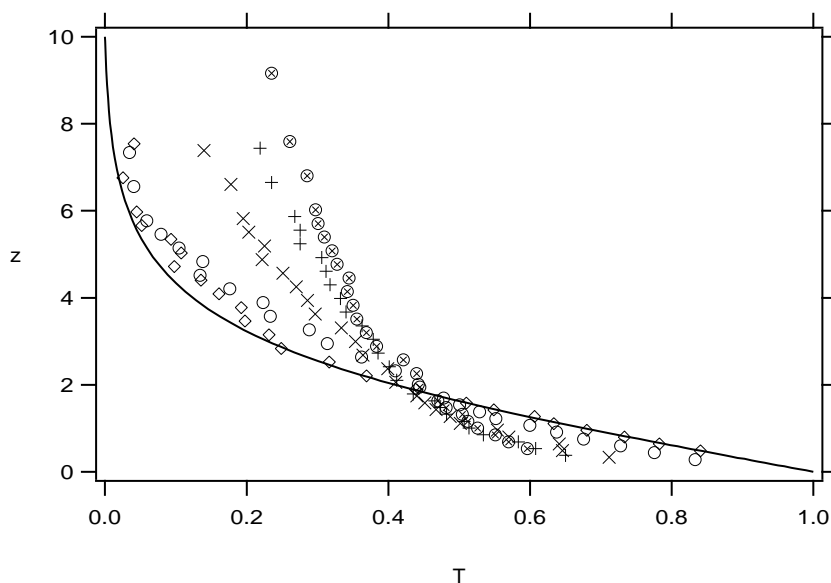


Figure 4.4: Measured temperatures at different r : $\diamond = 453$, $\circ = 502$, $\times = 527$, $+$ = 552 and $\oplus = 601$. The line is the theoretical solution for the laminar case.

As seen in fig 4.3 and 4.4 the velocity and temperature gradients at the wall seem to change at approximately the same radial position. This indicates that Reynolds analogy is valid at the wall for most of the disk surface, including most of the area where streamwise vortices are present in the flow over the disk. (The slope of the temperature profile, $\partial T/\partial z$ at $z = 0$, gives the heat transfer, the same is valid for the velocity profile and the drag: the larger the change of velocity/temperature with z , the larger the drag/heat transfer.) This can be concluded since it is already known that Reynolds analogy is valid in the laminar and turbulent region respectively.

4.2 Disturbance distributions and growth

In order to study how the heating of the disk surface influenced the disturbances, measurements were made with the hot wire positioned as in figure 4.5 at a height of approximately 0.5 mm. At this height, there was a maximum in the disturbance amplitude for the smallest radius. For larger radii, the maximum had not moved far, less than $50 \mu m$ up or down. The hot-wire signal was sampled and compensated for the different temperatures. This was done by compensating with different air temperatures for the three heated cases until the mean velocities were in as good agreement as possible with the mean velocity measured with no heating applied. It was assumed that the velocity or temperature profile did not change because of the heating. These mean velocities are shown as a function of the radius in figure 4.6. From these signals, the disturbance amplitudes shown in figure 4.7 have been calculated. As can be seen, the

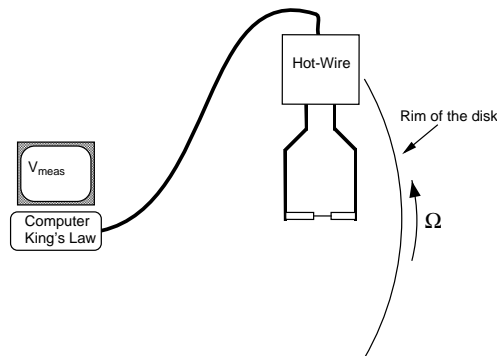


Figure 4.5: Hot-wire position for the measurements reported in figures 4.7, 4.8, 4.9, 4.10 and 4.11.

growth characteristics do not differ a lot for the different disk temperatures.

If the data from many rotations of the disk are phase-averaged (rotational-averaged) before the disturbance amplitudes are calculated, the results shown in figure 4.8 are obtained. If figure 4.8 is compared with figure 4.7, it can be concluded that the stationary character of the disturbances is much smaller for the heated case than in the unheated case, since unsteady disturbances will cancel each other in the averaging that has been done before the *rms*-values in figure 4.8 were calculated. This indicates that other factors than the roughness of the disk surface play an important role in triggering the disturbances when the disk is heated. Buoyancy could be such a factor.

In figures 4.9 and 4.10, velocity signals for different radial positions for the unheated and heated case are shown. By comparing the velocity signals for $r^*=0.13$ m it is clearly seen that initially the disturbance is larger and more homogeneously distributed round the disk for the unheated case than for the heated case.

For larger radii it is seen that the amplitude develops in different ways for the heated and unheated cases. In the heated case, secondary instabilities are clearly seen as kinks in the signal for $r^*=0.15$ m. In the unheated case, there are almost no kinks in the signal, even for $r^*=0.16$ m. In both cases, the flow is turbulent at $r^*=0.17$ m. Also, at $r^*=0.16$ m, the almost harmonic oscillation of the signal from the flow over the heated disk has little resemblance with the disturbed signal for the heated case at the same radial position.

The velocity signals shown in figures 4.9 and 4.10 show that the disturbance from the non-orthogonality between the disk and its axis is dominant up to a radius of 0.14 m. The amplitude of this disturbance is approximately 1.5 % of the disk speed at $r^*=0.1$ m. Since the slope of the tangential velocity gradient (see figure 4.1(b)) is around one, the movement of the disk in the vertical direction should be around 1.5 % of one vertical length unit under present conditions. One length unit at 1400 rpm is approximately 0.3 mm and 1.5 % of this is about 5 μm , a value in good correspondence with the measured value of the out of flatness of

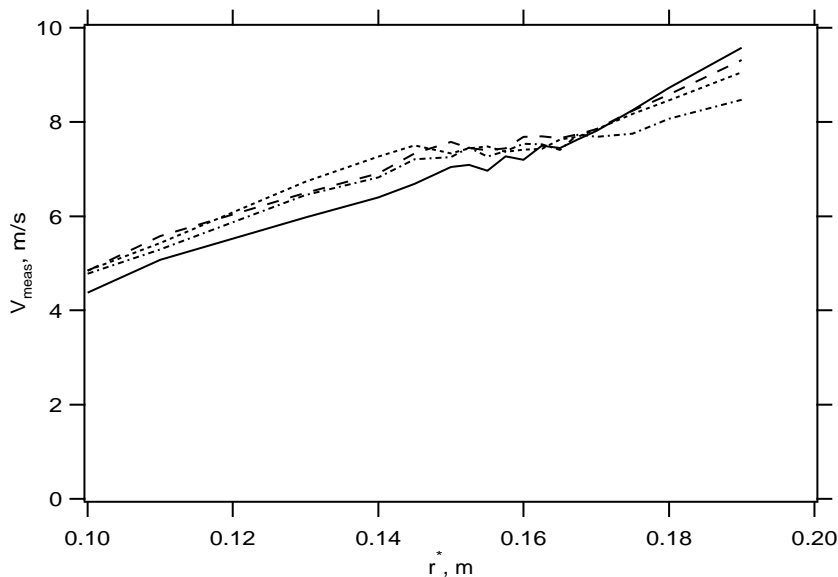


Figure 4.6: Mean values of V_{meas} after temperature compensation. The disk temperature is 0, 10, 20 and 40 K over room temperature for the solid, dashed, dotted and dash-dotted line, respectively.

the disk mentioned in chapter 3.

As can be seen in the spectra shown in figure 4.11, the frequency distributions do not differ much except at $r^* = 0.16$ m where the signal from the flow over the heated disk has a larger amount of energy at high frequencies, indicating a more turbulent flow at this stage. The spectra are taken from the signal corresponding to two rotations of the disk. This indicates that the propagation velocity and wavelength of the unsteady disturbances are such that the frequency measured by the hot wire fixed to the laboratory is the same as the frequency which is given by the steady vortices, that is seen in the spectra as the large peak near $\omega/\Omega=30$.

The actual frequencies and propagation velocities of the unsteady disturbances cannot be measured with one single probe fixed to the laboratory. From rotational-averaged velocity and temperature measurements, the disturbance distributions for disturbances stationary to the disk can be calculated. Such distributions for the circumferential velocity are shown figure 4.12 together with eigenfunction obtained in chapter 2.2. As can be seen in figure 4.12, there is a large discrepancy between the measured distribution and the theoretical prediction. The explanation to this deviation is given below.

As can be seen in figure 4.9, the low frequency disturbance arising from the skewness of the disk is dominant up to fairly high radii. For this reason, it can be expected that the disturbance distributions shown in figure 4.12a arises from the non-orthogonality between the disk and its axis. As can be seen in that figure, the disturbance distribution actually follows the derivative of the

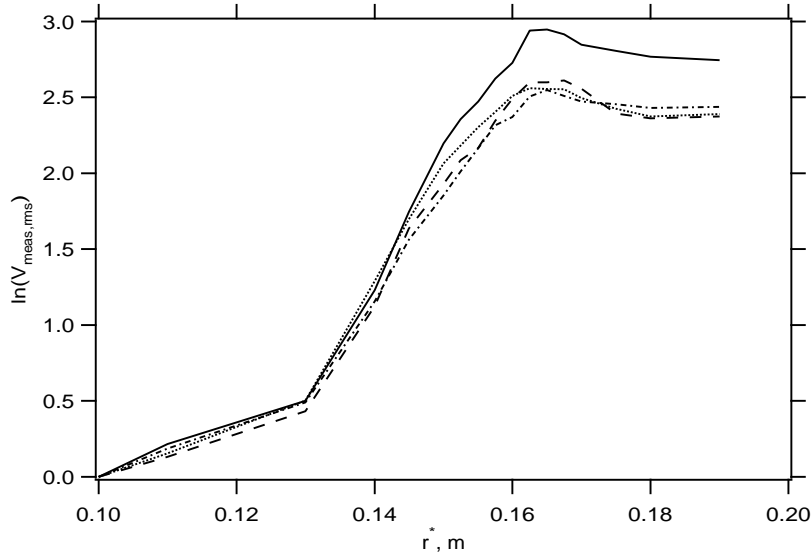


Figure 4.7: Disturbance growth for V_{meas} . The disk temperature is 0, 10, 20, 40 K over room temperature for the solid, dashed, dotted and dash-dotted line respectively.

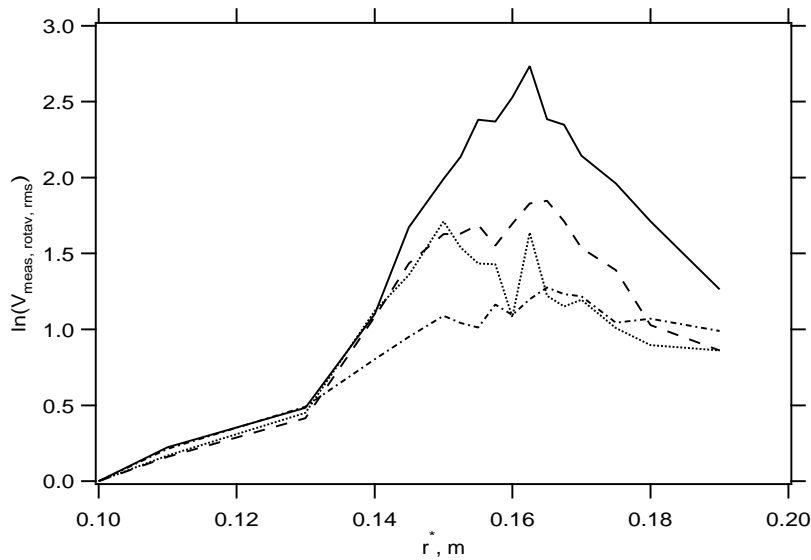


Figure 4.8: Disturbance growth for rotational-averaged V_{meas} . The disk temperature is 0, 10, 20 and 40 K over room temperature for the solid, dashed, dotted and dash-dotted line, respectively.

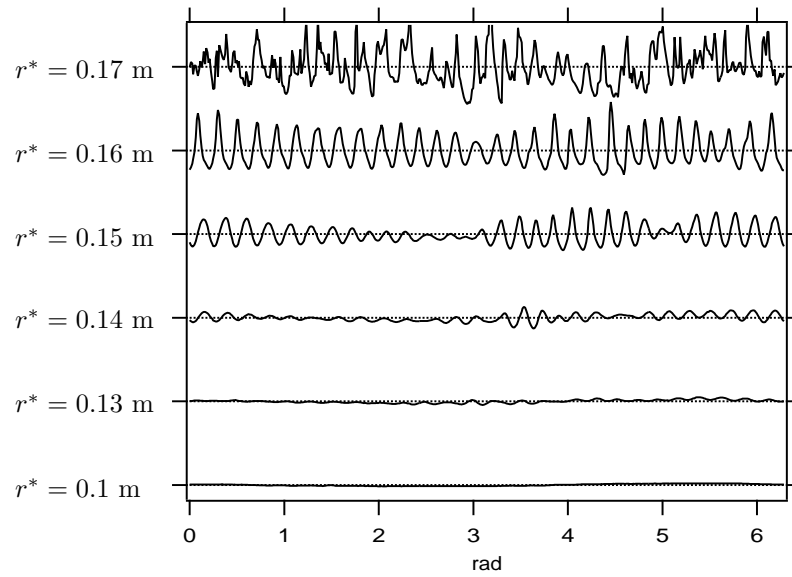


Figure 4.9: Velocity signals used for the results shown in figures 4.7, 4.8 and 4.11. The signals correspond to one revolution of the disk and are taken with no heating applied at 1400 rpm.

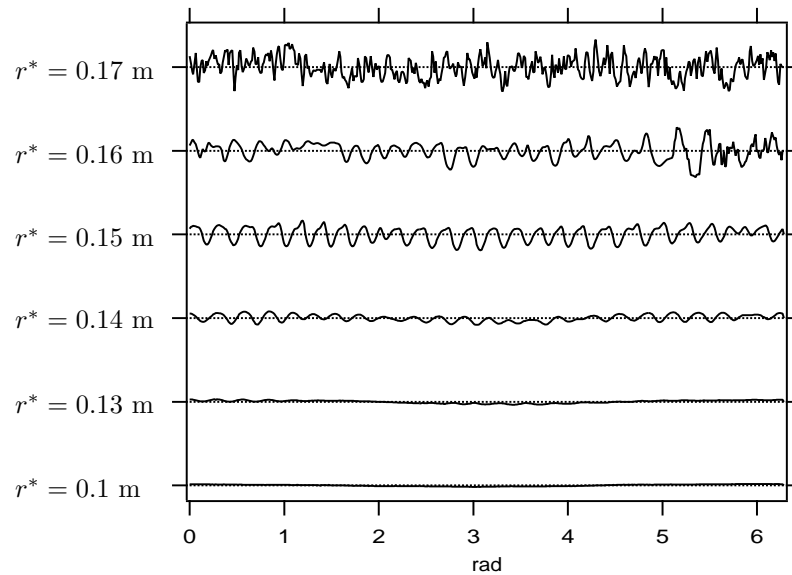


Figure 4.10: Same as for figure 4.10 except that the disk temperature is 40 K warmer than the temperature far away from the disk.

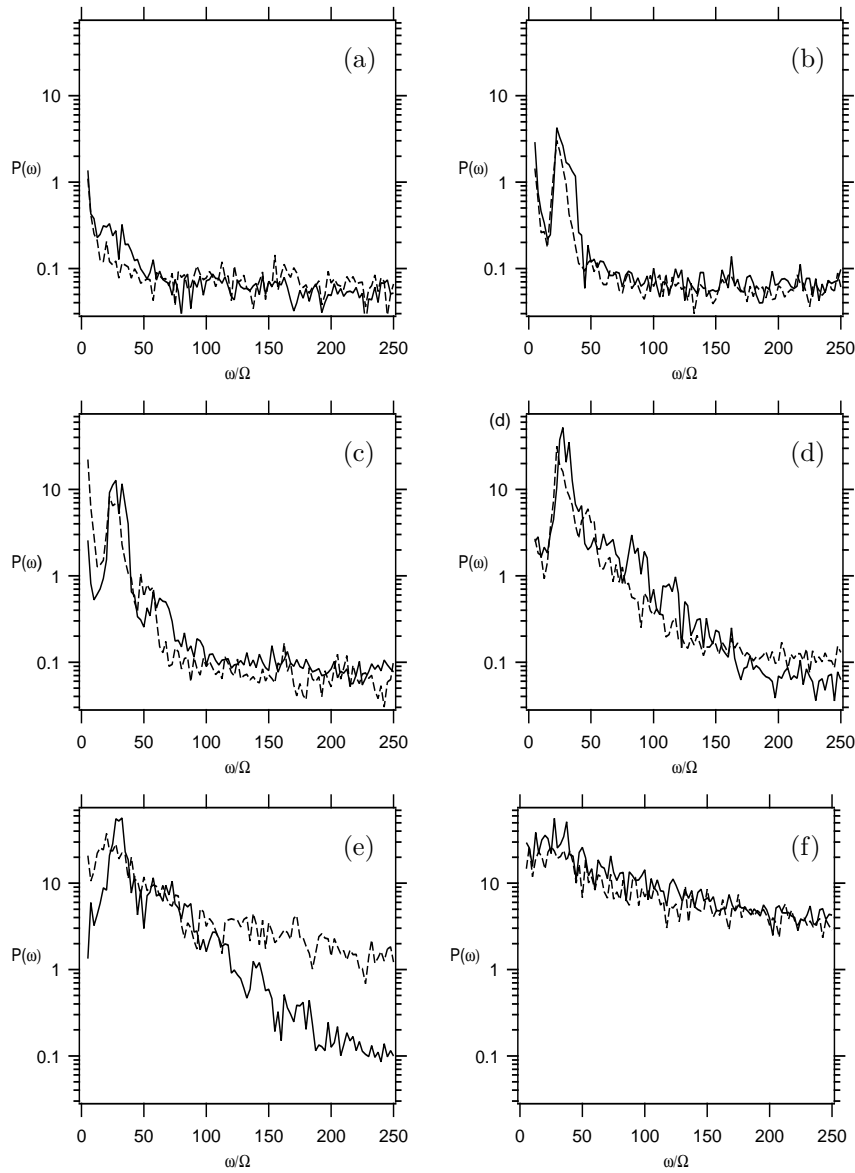


Figure 4.11: Frequency spectras for the velocity signal 0.5 mm over the disk for the unheated disk (solid) and when the temperature of the disk is 40 K over ambient temperature (dashed). The rotating speed is 1400 rpm and the radial position 0.1 m, 0.13 m, 0.14 m, 0.15 m, 0.16 m and 0.17 m from (a) to (f).

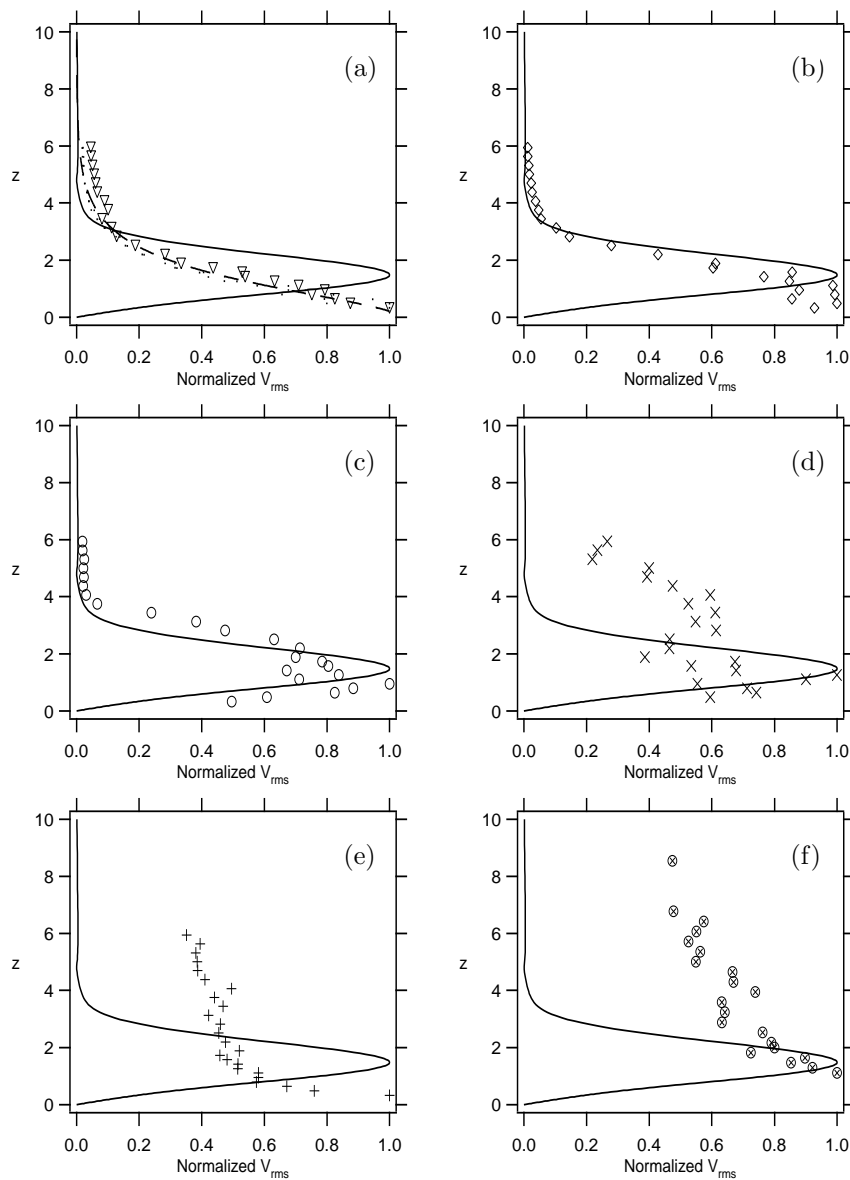


Figure 4.12: Measured disturbance distributions calculated from rotational-averaged velocity data compared with the eigenfunction of the stationary ($\omega_r = 0$) eigenfunction with the highest temporal amplification (largest ω_i) at $R = 300$, $\alpha = 0.382$, $\beta = 0.0774$ and $\omega_i = 0.000600i$. The non-dimensional radii for the measurements are: 249, 311 (\dots) and 374 (∇) in (a) and 436, 468, 499, 561 and 638 from (b) to (f).

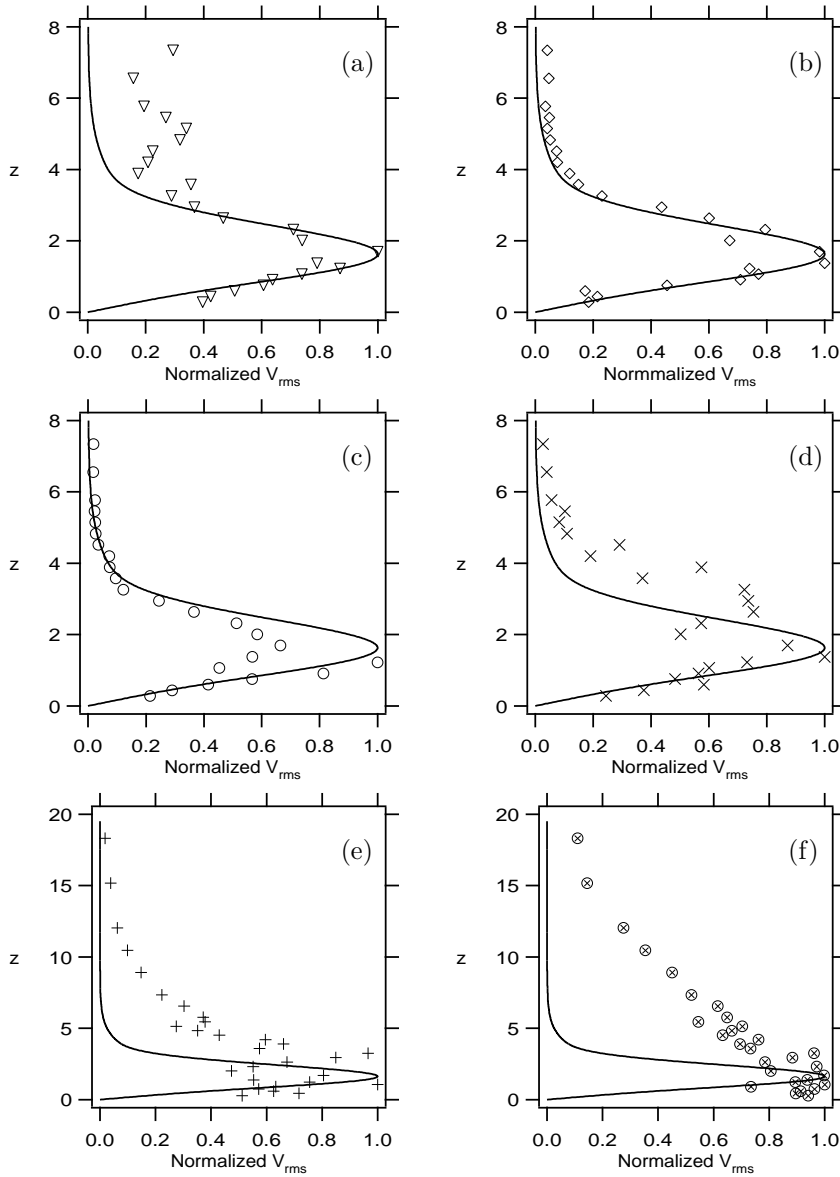


Figure 4.13: Measured disturbance distributions calculated from rotational-averaged temperature data compared with the eigenfunction of the stationary ($\omega_r = 0$) eigenfunction with the highest temporal amplification (largest ω_i) at $R = 300$, $\alpha = 0.382$, $\beta = 0.0744$ and $\omega_i = 0.000600i$. The non-dimensional radii for the measurements are: 352, 402, 453, 502, 527 and 552 from (a) to (f).

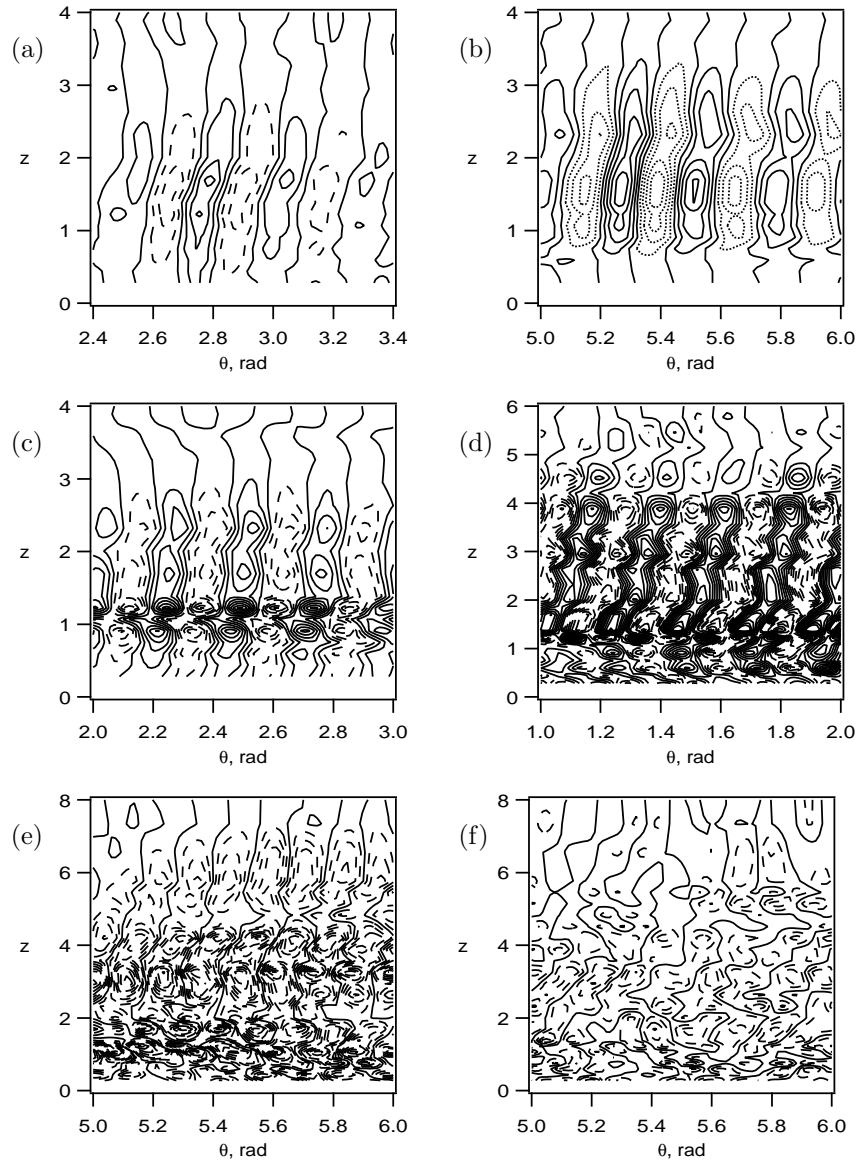


Figure 4.14: Contour plots of the temperature in the $z\theta$ -plane. The nondimensional radii is 352, 402, 453, 502, 527, 552 from (a) to (f). To obtain the physical picture, the plots should be stretched in the θ direction by a factor ranging from 64 to 113 in the different plots.

velocity. This is the expected distribution since the hot wire measures the velocity at varying height over the disk as the disk is rotating.

In order to avoid disturbances arising from the skewness of the disk, the temperature data was digitally high-pass filtered before further processing. As can be seen in 4.13, the resulting temperature distributions shows good correspondence to the theoretical eigenfunction at radii where the flow is critical but not absolute unstable, i.e. for $285 < R < 507$.

When the non-dimensional radius is increased further, both the temperature and velocity disturbance distributions develop a two-peak structure due to the vortices and as the flow becomes fully turbulent, the disturbance is more homogeneously distributed through the boundary layer.

In figure 4.14 the temperature disturbance are shown in a $z\theta$ -plane. Here it is clearly seen that the disturbances develop a two-peak structure as the radius increases. The number of vortices with no heating applied is around 30, as in previous investigations. However, with heating applied the number of vortices seem to decrease and with a disk temperature 40 K over the ambient air, the number of vortices on the disk is around 26.

4.3 Liquid crystal visualization

The flow above the heated rotating disk can be divided into three different regions depending on the character of the flow. From the centre and outwards we have called them the laminar region, the vortex region and the turbulent region.

With the temperature sensitive crystal film the decreased or increased surface temperature of the disk is visualized. The flow field is only indirectly visualized by this method. The blue colour is the warmest, the red colour is the coldest and in between there exists three different green shades.

In figure 4.16 for 1800 rpm a fairly sharp difference between two colours of the temperature sensitive crystal in the radial direction can be seen. For this case the colour difference occurs around $r^* = 142 - 144$ mm. This is the boundary between the vortex region and the turbulent region on the disk, which we from now on denote the turbulence front. In the turbulent part of the flowfield the heat transfer from the disk increases and cools down the surface of the disk more rapidly, than the vortex part of the flowfield. These visualizations were repeated with the angular velocity ranging from 1200 to 2000 rpm and the non-dimensional radial position of the temperature difference was found to be $r = 510$ with a small scatter around this value.

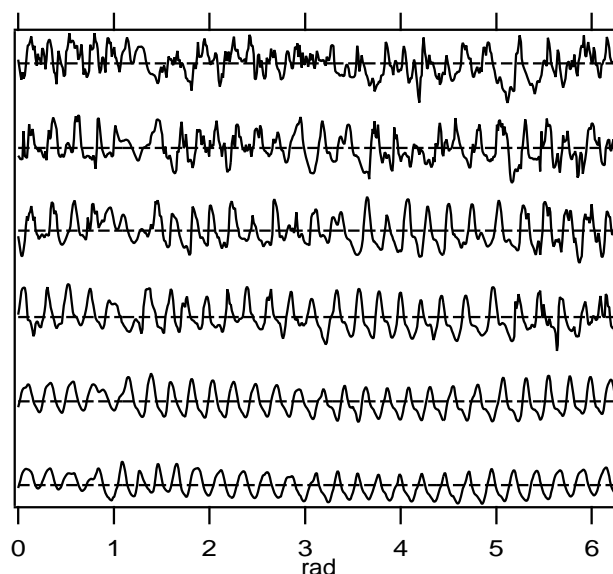


Figure 4.15: Normalized velocity signals from hotwire measurements for $r^* = 138, 140, 142, 144, 146$ and 148 mm, with decreasing radius downwards in the figure.

In figure 4.15 single realizations of normalized hot-wire signals for 1800 rpm at different radial positions are shown including the whole turbulence front in figure 4.16. The turbulence front is located between $r^* = 142$ and $r^* = 144$. At the smaller radii the vortex patterns in the hot-wire signal can clearly be seen, but as the radius increases secondary instabilities appear as kinks. Even further out turbulent spots appear near the front and finally a complete breakdown to turbulence occurs. As the character of the velocity signal is the main interest there is no need for calibrating the hotwire and as the drift of the hot-wire is not relevant the more robust tungsten wire was used.

In smoke visualizations like the one in figure 1.1 the stationary vortices, which appear as a smoke pattern on the disk, can be seen. This is also possible with the crystals as the vortices influence the heat transfer. Inside the turbulence front in figure 4.16 there is a vortex region and here a striped curved pattern is observed, which is due to a variation in cooling originating from the vortices. This effect of the vortices comes from the fact that cold air from above force hot air near the disk surface upwards in a circular motion. The vortices are stationary to the disk, which means that it is possible to capture the pattern by a camera using stroboscopic light.

In figure 4.17 for 1800 rpm two roughly cylindrical surface roughnesses have been introduced. The surface roughness consists of a claylike substance with an approximately constant diameter of 4.5 mm and with a height of 0.4 mm, which can be easily changed. Behind each roughness a wake appears and the turbulence front moves towards smaller radii. Initially the wake probably consists of two counter-rotating vortices. As the vortices, that occur without roughness,

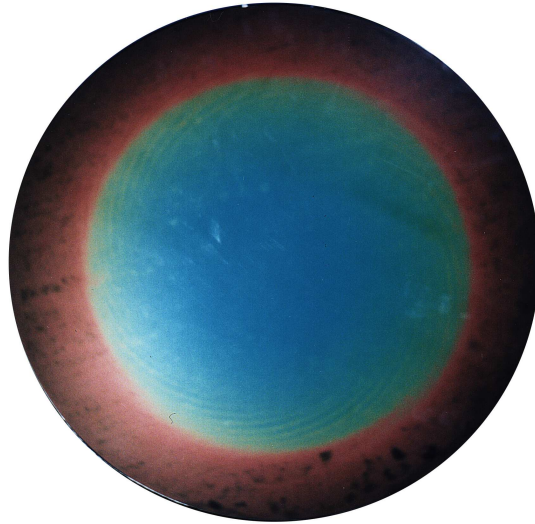


Figure 4.16: Temperature sensitive crystal visualization for 1800 rpm.

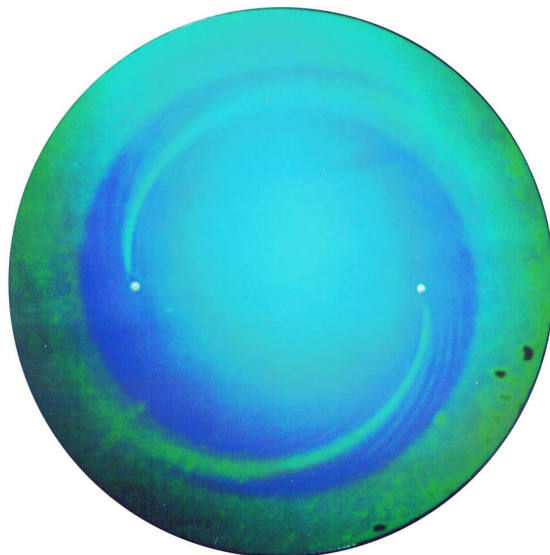


Figure 4.17: Temperature sensitive crystal visualization for 1800 rpm with two surface roughness elements, which have a height of 0.4 mm.

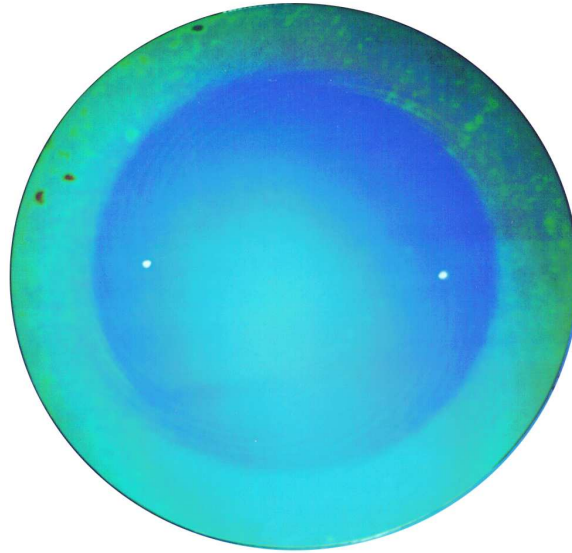


Figure 4.18: Temperature sensitive crystal visualization for 1800 rpm with two surface roughness elements, which have a height of 0.08 mm.

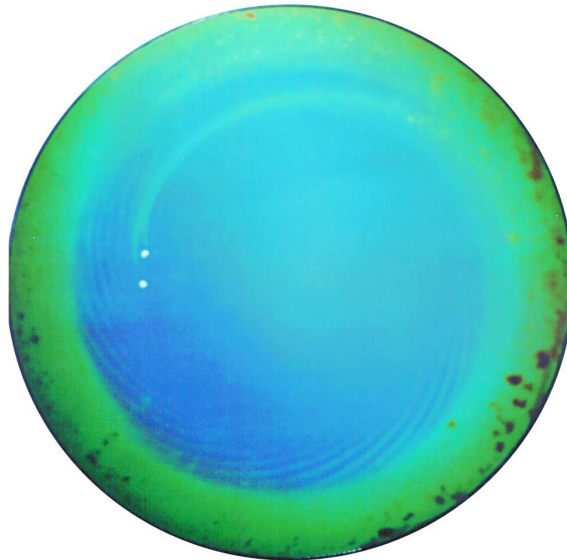


Figure 4.19: Temperature sensitive crystal visualization for 1800 rpm with two surface roughness elements which have a height of 0.4 mm, where one of the elements trails the other.

are co-rotating one of the wake vortices dies out and the other one survives increasing the heat transfer from the disk surface.

Figure 4.18 for 1800 rpm shows a visualization when the height of the roughnesses are 0.08 mm. Here there are no wakes behind the roughnesses and the result resemble that in figure 4.16. Obviously the height of the roughnesses are important when considering the influence on the heat transfer. The figures 4.17 and 4.18 evidently show the existence of a threshold for the height of the roughnesses to increase the heat transfer, which has also been pointed out by Jacobi & Shah (1995).

In figure 4.19 for 1800 rpm the position of the roughnesses and the effect on the heat transfer are investigated. The second roughness is placed behind the first one at the same radius. The wakes behind the roughnesses grow to one wake and increase the heat transfer in a larger region than in the one roughness case.

A peculiar phenomenon observed is that outside the surface roughness, at almost the same circumferential position as the roughness, the turbulence front is pushed further out in the radial direction. A possible explanation is that the roughness element changes the velocity profile in such a way that the onset of the absolute instability moves outward, but in order to fully explain this phenomena, more investigations are needed.

Chapter 5

Discussion

5.1 Air velocity and temperature measurements

This study is focused on the flow structure near the surface of a rotating disk. In the rotating-disk flow the large velocities are dominant near the surface and higher up in the boundary layer the velocities gradually decrease. The smaller velocities are more easily influenced by disturbances from the surrounding environment and generally speaking it is in the upper part of the boundary layer that the measured results deviate in comparison with theory.

An existing problem that affects the hot-wire measurements, when using a probe fixed to the laboratory frame, is the non-orthogonality between the rotating disk and its axis. This skewness becomes a dominant disturbance in the disturbance distribution when the flow disturbances not yet have developed.

There is a good agreement between the measured laminar velocity profiles and their respective theoretical similarity solutions, that can be seen in figures 4.1. The deviation from theory can be found in the upper part of the boundary layers where the velocities are small. This deviation is mostly due to the deviation that occurs when small velocities are measured and the hot-wire sensitivity equation 3.2 is used. No compensation for the small axial velocity component has been done and this can also cause small deviations. Since the radial velocity is lower than the tangential velocity the disturbances described above affect the measurements of the radial velocity more.

A good agreement can also be found in the measured laminar temperature profiles in comparison to the theoretical similarity solution, seen in figure 4.2. As for the velocities, the deviations take place in the upper part of the boundary layer probably due to errors in measuring the ambient air temperature together with the temperature variations in the ambient air approaching the disk.

The flow fields become transitional and finally turbulent when the radius increases. This scenario is captured in the profiles for the tangential velocity and the temperature, which deviate from the laminar ones and become fully turbulent, as seen in figures 4.3 and 4.4. This means that the velocity gradient

(dV/dz) and the temperature gradient (dT/dz) , which are proportional to the drag and the heat transfer respectively, increase rapidly in the same region. The conclusion is that there is no region in the disk flow with large heat transfer and low drag.

To check whether the flow is influenced by different disk temperatures a study of the disturbance amplitude growth with increasing radius has been made. Considering the character of the disturbance amplitude growth without averaging, the temperature difference does not affect it, as can be seen in 4.7. However the effect becomes apparent when the signal is rotational averaged before the amplitudes of the disturbances are calculated. Doing this the stationary character is enhanced and the fluctuating part of the signal is suppressed. In this case it is obvious from comparing figures 4.7 and 4.8 that the stationary character is smaller in the heated case.

In figures 4.9 and 4.10 the hot-wire signals corresponding to one revolution for different radii with $\Delta T = 0$ K and $\Delta T = 40$ K, are shown. In both cases the skewness of the disk can be seen. It is important to remember that the signals are peak-normalized and the disturbance caused by the skewness in reality becomes less dominant when the radius is increased and the flow disturbances become more dominant. Nevertheless the disturbance from the skewness is dominant up to at least $r^* = 0.14$ m. The stationary vortices or primary instabilities and the kinks or the secondary instabilities can also be seen and they appear earlier in the heated case.

One parameter not considered in the theoretical analysis is the buoyancy. The buoyancy can affect the triggering of the disturbances in the disk flow. As concluded from the disturbance growth the primary instabilities seen in figure 4.10 are not completely stationary. This indicates that instabilities with $\omega_r \neq 0$ by buoyancy. It is known from e.g. Balachandar *et al.* (1992) that there exist non-stationary disturbances with larger growth rates than the stationary disturbances. If such non-stationary disturbances are triggered by buoyancy this could be an explanation to the observation from figures 4.9 and 4.10 that secondary instabilities are more developed in the heated case than in the unheated case.

In the frequency distribution figure 4.11 of the above mentioned hot-wire signals the heating effect appears only in the measurements for $r^* = 0.16$ m, where there is more energy at high frequencies for the heated case. This indicates that transition is a more convective process in the heated case than in the unheated case. The stationary vortices is seen as a large peak around $\omega/\Omega = 30$.

After high-pass filtering in order to filter away disturbances from the non-orthogonality between the disk and its axis, a good correspondence between measured temperature disturbance distributions and results from linear stability theory has been obtained for a limited range of radii, as can be expected since the disturbances decay for smaller radii and the flow becomes turbulent at larger radii.

As has been reported in 4.2, the number of vortices seems to decrease with heating applied as compared to the case without heating. A possible explanation to this phenomenon could be that with heating applied, a buoyancy instability

is present and triggers the vortices, rather than stationary imperfections that triggers the vortices when no heating is applied.

5.2 Liquid crystal visualizations

In the liquid crystal visualizations, the heating was cut off when the disk had been heated to the desired temperature and after this, the disk cooled because of the convection. It can be seen in the photographs shown in figures 4.16–4.19 that under these circumstances, there is a distinct temperature difference between the laminar and turbulent region. This is seen as a colour change of the liquid crystals.

The hot-wire signals in figure 4.15 shows that the position of this surface-temperature decrease is close to the transition position. The radial position of the temperature decrease is $r = 510$ (using room temperature viscosity) with a small scatter around this value for different rotating speeds between 1200 and 2000 rpm (the scatter is less than one percent). This is tantalizingly close to the value 507 where the absolute instability should trigger transition according to Lingwood (1997a).

From the photographs it can also be concluded that the stationary vortices seen in smoke visualizations such as figure 1.1 changes the disk temperature locally (because of locally varying heat transfer). This is seen as a striped pattern prior to the temperature decrease in the photographs. The amplitude of this striped local temperature variation depends on both the amplitude of the linear primary disturbances and the heat conductivity of the liquid crystal film.

If the flow is subject to a disturbance of sufficient amplitude, by e.g. a large enough roughness element, the surface temperature decreases in a wake behind this element. If the wake is studied in detail, it can be seen that initially it consists of two or more stripes but further downstream, one of these develop more than the others. The stripes seen initially are probably due to vortices and separation bubbles but as the disturbances develop downstream, the most amplified disturbances are the ones similar to the naturally occurring disturbances, i.e. corotating vortices. For this reason, vortices rotating in the other direction are suppressed.

The radial position of the temperature decrease did not change much because of the disturbance element, and when it did, it was positioned further *out* than in the undisturbed case. This indicates that the transition scenario for the flow does not change much due to the introduced disturbance. Studying the wake, it can be seen that the leading edge spirals outwards and crosses the temperature decrease under an angle. However, observing the trailing edge of the disturbance, it is clear that it approaches the temperature decrease under an angle. This behaviour of the trailing edge of a wave-packet is the behaviour described by Lingwood (1996) for a flow that is subject to an absolute instability.

The experiments where the height of the roughness element was varied show, that if a large enough roughness element is applied to the surface, heat transfer can be increased in a wake behind this element. By applying many elements

around the disk it should be possible to increase heat transfer for the whole of the disk surface outside these elements. If the Reynolds number where the elements are applied is undercritical, the disturbances might decay and a new set of elements will be needed to increase the heat transfer all the way out to the turbulence front.

It is also clear that there exists a threshold height of the elements if the heat transfer is to be increased behind them. Those experiments were made at one rotating speed and one radial position for the roughnesses only (namely 1800 rpm and $r^* = 0.1$ m). This threshold height seemed to be around 0.4 mm, i.e. 1.4 length units in the nondimensional axial coordinate. This is a value in close agreement with the observations of Jacobi & Shah (1995) that the height of the roughness element has to be of the same magnitude as the boundary layer thickness in order to effect the heat transfer.

Theodorsen & Regier (1948) observed that roughness on the disk surface only changed the non-dimensional radius for the rapid increase of drag towards the centre of the disk. From the liquid crystal visualizations, it was observed that a large enough roughness element increases the heat transfer from the disk to the air from the element and out. Such a possibility could be very important in some applications, e.g. the micro-gravity evaporator studied by Rahman & Fahgri (1992).

Acknowledgements

First of all we would like to thank our parents for their support and encouragement throughout our lives.

We thank our supervisors, prof. Y. Kohama at Tohoku University and prof. H. Alfredsson at Royal Institute of Technology for their help, professional as well as personal.

The encouragement and instructions received from Dr. M. Matsubara has been invaluable.

The practical help received from Mr. Akama, Mr. Hayasaka and Mr. F. Ohta regarding the equipment and their handling has also been very valuable.

We also thank Dr. M. R. Ahmed, Dr. Y. Egami, Dr. B. Faycal and Dr. H. Watanabe for their help and encouragement during the work.

Most of the work was performed at the Institute of Fluid Science, Tōhoku University, Sendai, Japan where the support, help and heartiness we received from the staff and the students at Kohama Laboratory made our stay in Japan enjoyable and productive. Thank you very much, we will never forget you.

A very special thank to Dr & Mrs M. Kobari together with Tetsu and Reiko for sharing their family spirit with us.

We would also like to thank the staff in the fluid mechanics laboratory at Royal Institute of Technology, Stockholm for support and help during the writing.

Alex wants to thank his family and friends for their warm support and encouragements during the stay in Japan. From the bottom of my heart thank you Katarina, Rosie, Marie, Stefan, Richard, Peter, Johan, Lillen. I also want to send a thought to my dear and unfortunately deceased grandmother Märta Cederholm, who always have supported me during my years in education.

Fredrik wants to thank some of the friends and family supporting him via personal visits, letters or e-mails during the stay in Japan. Thank you Albin, Alicia, Anders, David, David, Gustaf, Gitte, Henrik, Johan, Lena, Lovisa, Maria, Maria, Mia, Ola and Olle. Fredrik also wants to thank the staff and management at Boghammar Marin for the skills and attitude he developed there.

Economical support for the stay in Japan was received from the Gadelius' foundation (AC), the Sasakawa foundation (FL), the School of engineering physics at KTH and the Anna Whitlock's memorial foundation.

Appendix A

Numerical methods

This appendix considers the numerical analysis used to solve the governing equations along with the boundary conditions for the velocity disturbance and the temperature disturbance, where the numerical method is based on Malik (1985).

Equations (2.17) and (2.18) can be represented as a system of first order equations with a system matrix \mathbf{A} as follows.

$$\frac{d\vec{\phi}}{dz} = \mathbf{A}\vec{\phi}, \quad \vec{\phi} = (\phi_1, \phi_2, \phi_3, \phi_4, \phi_5, \phi_6)^T \quad (\text{A.1})$$

where

$$\begin{aligned} \phi_1 &= \tilde{w} & \phi_2 &= \frac{d\phi_1}{dz} & \phi_3 &= \frac{d\phi_2}{dz} \\ \phi_4 &= \frac{d\phi_3}{dz} & \phi_5 &= \alpha\tilde{v} - \beta\tilde{u} & \phi_6 &= \frac{d\phi_5}{dz} \end{aligned} \quad (\text{A.2})$$

In this way it is possible to solve the problem by for example a Runge-Kutta or finite difference method. By means of the Euler-Maclaurin formula a fourth order finite difference scheme is derived and is used to solve the system (2.17) and (2.18) together with the boundary conditions (2.20).

$$\psi^k - \psi^{k-1} = \frac{1}{2}y_k\left(\frac{d\psi^k}{dz} + \frac{d\psi^{k-1}}{dz}\right) - \frac{1}{12}y_k^2\left(\frac{d^2\psi^k}{dz^2} - \frac{d^2\psi^{k-1}}{dz^2}\right) + O(y_k^5) \quad (\text{A.3})$$

where

$$\psi^k = \vec{\phi}(z_k), \quad y_k = z_k - z_{k-1} \quad (\text{A.4})$$

To be able to resolve the system the following node distribution is used

$$z_k = \frac{L(k-1)}{Ns - (k-1)} \quad (k = 1, 2, \dots, N+1) \quad (\text{A.5})$$

where z_∞ is the far away boundary, L is a scaling parameter, $s = 1 + L/z_\infty$ and N is the number of nodes in the computational domain. The values used are 20, 1.8 and 200 for z_∞ , L and N respectively.

With the finite difference scheme the following matrix equation is obtained for each level containing two node values. All matrices \mathbf{A}_k , \mathbf{B}_k and \mathbf{I} are 6×6 matrices, where \mathbf{I} is the identity matrix.

$$\begin{aligned} [\mathbf{I} - \frac{1}{2}y_k\mathbf{A}_k + \frac{1}{12}y_k^2\mathbf{B}_k]\vec{\phi}^k - [\mathbf{I} + \frac{1}{2}y_k\mathbf{A}_{k-1} + \frac{1}{12}y_k^2\mathbf{B}_{k-1}]\vec{\phi}^{k-1} = 0 \\ (k = 2, 3, \dots, N+1) \end{aligned} \quad (\text{A.6})$$

Above \mathbf{A}_k and \mathbf{B}_k are the matrices for node k . The components $(\mathbf{B})_{ij}$ of \mathbf{B} is given by

$$(\mathbf{B})_{ij} = \frac{d(\mathbf{A})_{ij}}{dz} + \sum_{l=1}^6 (\mathbf{A})_{il}(\mathbf{A})_{lj} \quad (\text{A.7})$$

The above equation system (A.6) for each node pair along with the boundary conditions (2.20) are written in block tridiagonal form.

$$\mathbf{L}\Phi = \mathbf{0}, \quad \Phi = (\vec{\phi}_1, \dots, \vec{\phi}_{N+1})^T \quad (\text{A.8})$$

The system (A.8) can now be solved, but to avoid trivial solutions the system is made inhomogeneous by replacing the imposed boundary condition at the disk surface $\phi_1(0) = 0$ with $\phi_3(0) = 1$. It is now possible to solve the system and with Newton's method an iteration for the unknown quantities to fulfil $\phi_1(0) = 0$, can be made. The unknown quantities are the eigenvalues, which are called $\{x, y\}$.

$$\begin{aligned} \phi_{1r}(0) + \frac{\partial\phi_{1r}(0)}{\partial x}\Delta x + \frac{\partial\phi_{1r}(0)}{\partial y}\Delta y = 0 \\ \phi_{1i}(0) + \frac{\partial\phi_{1i}(0)}{\partial x}\Delta x + \frac{\partial\phi_{1i}(0)}{\partial y}\Delta y = 0 \end{aligned} \quad (\text{A.9})$$

The derivatives with respect to x and y are calculated by taking into account (A.8) and differentiate this relation with respect to x and y .

$$\begin{aligned} \mathbf{L}\frac{\partial\Phi}{\partial x} = -\frac{\partial\mathbf{L}}{\partial x}\Phi \\ \mathbf{L}\frac{\partial\Phi}{\partial y} = -\frac{\partial\mathbf{L}}{\partial y}\Phi \end{aligned} \quad (\text{A.10})$$

where

$$\{x, y\} \in \{\alpha_r, \beta_r\} \quad (\text{A.11})$$

Equation (2.24) is solved with finite differences using a symmetric node distribution. The following second order methods to represent the derivatives are used.

$$(\psi'')^k = \frac{\psi^{k+1} - 2\psi^k + \psi^{k-1}}{y_k^2} + O(y_k^2) \quad (\text{A.12})$$

$$(\psi')^k = \frac{\psi^{k+1} - \psi^{k-1}}{2y_k} + O(y_k^2) \quad (\text{A.13})$$

$$y_k = z_{k+1} - z_k = z_k - z_{k-1} \quad (\text{A.14})$$

Introducing equations (A.12) and (A.13) into equation (2.24) the result is expressed in the following form for each node level.

$$E_k^3 \phi_{k-1} + E_k^2 \phi_k + E_k^3 \phi_{k+1} = G_k \quad (\text{A.15})$$

where

$$\phi_k = \tilde{\tau}(z_k) \quad (k = 1, 2, \dots, N) \quad (\text{A.16})$$

The equation (A.15) for each node level along with the boundary conditions (2.25) are written as a system resulting in an almost tridiagonal system matrix \mathbf{E} and where \vec{G} is the inhomogeneous righthand side.

$$\mathbf{E}\Phi = \vec{G}, \quad \Phi = (\phi_1, \dots, \phi_N)^T, \quad \vec{G} = (G_1, \dots, G_N)^T \quad (\text{A.17})$$

The system A.17 can be solved and the eigenfunction $\tilde{\tau}$ can be obtained for specified α , β , ω , Pr and R .

Appendix B

Simple rim lift-up analysis

When the disk is heated from the bottom, the rim of the disk can be expected to warp because of the temperature gradient through the disk. In the present case this effect is fairly small, as can be seen from the analysis below.

The local Nusselt number from the disk is known to vary approximately as $Nu = 0.0188r^{1.6}$ [7] for turbulent flow. If $r^* = 200$ mm, $\Delta T = 20$ K and the rotating speed is 1400 rpm this gives a local heat transfer rate of 1.4 kW/m². In aluminium ($k = 238$ Wm/K) this gives the temperature gradient normal to the surface as $\partial T / \partial z = 6.1$ K/m. Finally the temperature difference between the horizontal surfaces for the present disk becomes 0.12 degrees. All material data has been taken from [26].

It is easy to derive an expression for the bowl radius of an infinite, circular plane with a temperature difference between its surfaces. The warmer surface is $\delta = l\kappa(T_{hot} - T_{cold})$ longer than the colder one where κ is the thermal expansion coefficient ($23.2 \cdot 10^{-6}$ K⁻¹ for aluminium) and l is the radius of the cold disk (see figure B.1). The easily derived expression is (see figure B.1) $\Re = hl/\delta$. The rim lift-up, γ , becomes $2\Re \sin^2(l/2\Re)$. In the present case, this gives a \Re of 7.1 km and a 2.8 μ m lift-up of the rim. This is probably an overestimate, since the heat transfer is smaller closer to the center of the disk than the value used above. Bearing this in mind, the value 2.8 μ m is encouragingly small. At 1400 rpm, the rotating speed most usually used in the experiments, 2.8 μ m corresponds to less than one percent of one length unit in the axial coordinate.

No measurements of the deflection of the disk while rotating or heated could be performed.

To justify the assumptions about the temperature gradient above some simple numerical simulations were done, see figure B.2. In those calculations, the steady heat-equation was solved for the interior of the disk. Assuming an axial symmetric heat radiation on the bottom of the disk, the problem becomes two-dimensional with the two coordinates: r , zero at the centre and one at the rim, and ζ , which is zero at the bottom surface of the disk and one on the upper surface.

On the bottom side, the boundary condition was chosen to simulate a circular

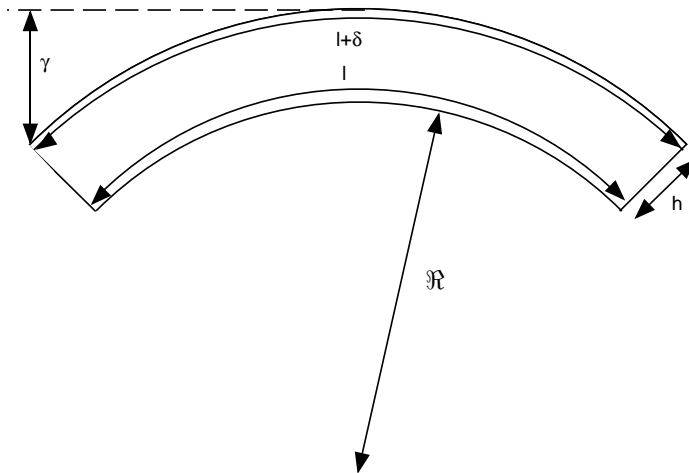


Figure B.1: Variable definitions for the simple rim-lift up analysis.

thin radiation source positioned below the disk (see figure B.3). On the upper surface of the disk, the heat transfer from the disk were taken from the values measured by Elkins & Eaton (1997) and on the rim of the disk, a suitable heat transfer coefficient was chosen. The effect of variations of the rim heat transfer coefficient was not very large.

As can be seen in figure B.2 the temperature difference between the bottom and upper side is close to the value 0.12 m estimated above.

A second reason for the numerical simulation of the temperature inside the disk was to investigate whether it was possible to achieve a close to isothermal temperature on the upper surface of the disk. As can be seen in figure B.2 the surface temperature only varies approximately 0.5 K in the radial direction. The variation of the temperature on the surface of the physical disk was somewhat higher.

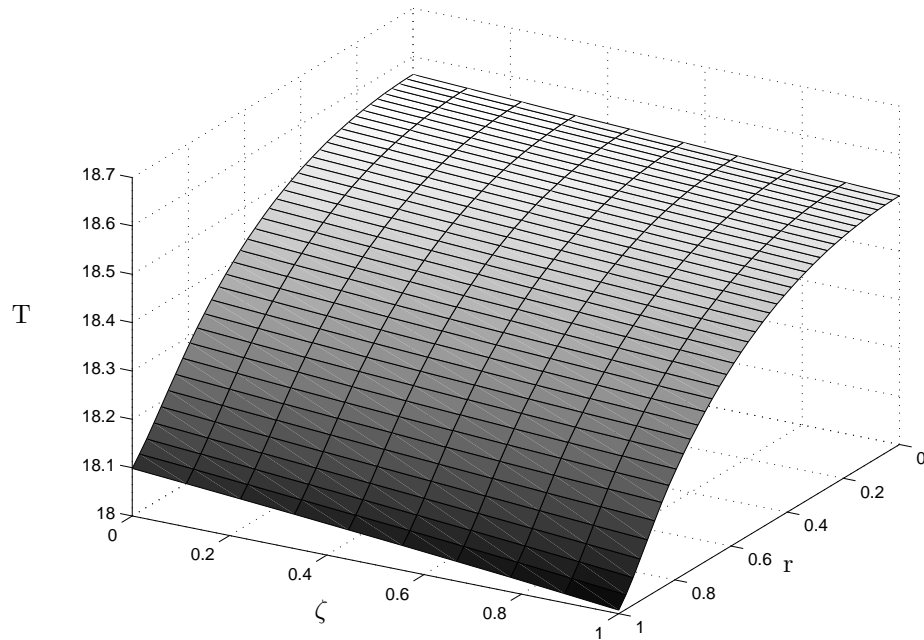


Figure B.2: Calculated temperature in the interior of the disk used in the present experiments. In the case shown, the diameter of the radiator ring shown in figure B.3 is the same as the disk and the ring is situated 0.1 m below the disk. The radiation power of the ring is 2 kW and the rotating speed of the disk is 1500 rpm.

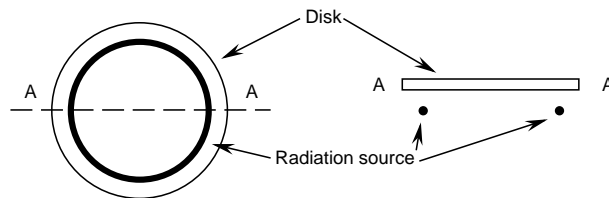


Figure B.3: The radiation source used in the calculation presented in figure B.2.

Appendix C

Single hot-wire multicomponent measurements

Here we study the following relation between the velocity measured by the hot-wire and the angle between the hot-wire and the flow direction:

$$U_{meas}^2 = U_\infty^2 (\cos^2 \phi + k^2 \sin^2 \phi) \quad (C.1)$$

or alternatively:

$$U_{meas}^2 = U_n^2 + k^2 U_t^2 \quad (C.2)$$

where U_n and U_t are the velocity components normal and tangential to the wire, respectively. In the present case, the parameter k varies with velocity as seen in figure C.1. In the figure, k has been calculated by a least square fit of (C.1) to directional sensitivity measurements made with the DISA calibration nozzle such as the one in figure 3.4 (the two figures are actually made from the same sets of data).

As can be seen in figure C.1, k is approximately 0.23 at large velocities which is close to the value of 0.2 typically obtained for hot wires with a length/diameter ratio of 200. From our tests, k seems to increase as the velocity is decreased. If the two velocity components are orthogonal and their instantaneous values are taken to be \tilde{U} and \tilde{V} , they can be decomposed into one stationary part and one fluctuating part as previously:

$$\tilde{u} = U + u \quad (C.3)$$

$$\tilde{v} = V + v$$

If the two wire directions used are parallel to the two velocity components directions, inserting (C.3) into (C.2) and time averaging (here denoted by overlined symbols) gives a set of two easily solved linear equations in $\overline{u^2}$ and $\overline{v^2}$ (i.e. u_{rms}^2

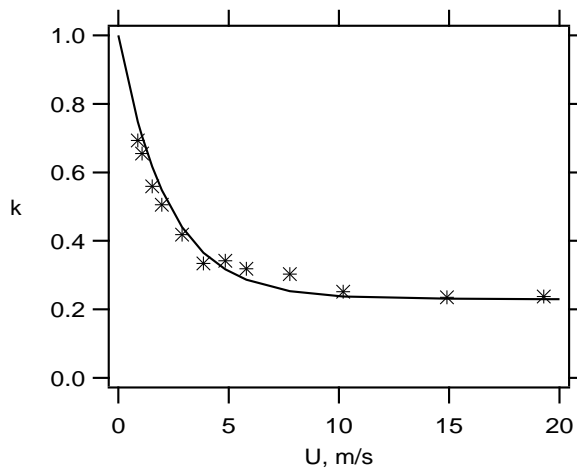


Figure C.1: The dependency of k on velocity. The stars are measured k values, the line is $0.77e^{0.45U} + 0.23$.

and v_{rms}^2):

$$\begin{aligned}
 U_1^2 + \bar{u}_1^2 &= U^2 + \bar{u}^2 + k^2 (V^2 + \bar{v}^2) \\
 U_2^2 + \bar{u}_2^2 &= V^2 + \bar{v}^2 + k^2 (U^2 + \bar{u}^2)
 \end{aligned}
 \tag{C.4}$$

where indices 1,2 denote the velocity signals from the two measurements. The wire is directed normal to the U-component during the first measurement and normal to the V-component during the second.

If, however, the two wire directions do not agree with the directions of the components, an additional measurement is needed. If the quantities U_n and U_t in (C.2) are expressed in $U + u$ and $V + v$, the cross-correlation \overline{uv} enters the equation after time averaging of the equations. This adds one unknown and consequently, one more measurement for a third orientation of the hot wire is required. Unfortunately only two angles were measured during the present measurements.

During the present work, the idea was to use the rotational-averaged velocity data and calculate the disturbance amplitude for those stationary to the disk with the method described in section 3.2. As can be seen in figure 4.12 the results from these measurements do not agree very well with the linear stability. Unfortunately no third measurement is available so we cannot use the method described in this appendix to calculate the disturbance amplitudes.

Bibliography

- [1] BALACHANDAR, S., STREETT, C. L. & MALIK, M. R. 1992 Secondary instability in rotating-disk flow. *J. Fluid Mech.* **242**, 323–347
- [2] BEJAN, A. 1995 Convection heat transfer. *John Wiley & Sons* U.S.A.
- [3] CEBECI, T. & ABBOTT, D. E. 1975 Boundary layers on a rotating disk. *AIAA J.* **13**, 829–832
- [4] CHAM, T-S & HEAD, M. R. 1968 Turbulent boundary-layer flow on a rotating disk. *J. Fluid Mech.* **37**, 129–147
- [5] COBB, E. C. & O. A. SAUNDERS 1953 Heat transfer from a rotating disk. *Proc. R. Soc. A* **236**, 242–351
- [6] DORFMAN, L. A 1963 Hydrodynamic resistance and the heat loss of rotating solids. *Oliver and Boyd*, Edingburgh
- [7] ELKINS, C. J. & EATON, J. K. 1997 Heat transfer in the rotating disk boundary layer. *Report No. TSD-103* Stanford University
- [8] FALLER, A. J. 1991 Instability and transition of disturbed flow over a rotating disk. *J. Fluid Mech.* **230**, 245–269
- [9] GREGG, J. L. & SPARROW, E. M. 1959 Heat transfer from a rotating disk to fluids of any Prandtl number. *J. Heat Transfer*, **C 81**, 249–251
- [10] JACOBI, A. M., SHAH, R. K. 1995 Heat transfer surface enhancement through the use of longitudinal vortices: a review of recent progress. *Exp. Thermal Fluid Science*, **11**, 295–309
- [11] JOHANSSON, A. V. & ALFREDSSON, P. H. 1982 On the structure of turbulent channel flow. *J. Fluid Mech.* **22**, 295–314
- [12] JOHANSSON, A. V. & ALFREDSSON, P. H. 1988 Experimentella metoder inom strömningsmekaniken. *Institutionen för Mekanik, KTH*, Sweden (*in Swedish*)
- [13] KÁRMÁN, TH. VON 1921 Über laminare und turbulente Reibung. *Z. Angew. Math. Mech.* **1**, 233–252 (*in German*)
- [14] KOBAYASHI, R., KOHAMA, Y., & TAKAMADATE, CH. 1980 Spiral vortices in boundary layer transition regime on a rotating disk. *Acta Mechanica*, **35**, 71–82

- [15] KOHAMA, Y. & KOBAYASHI, R. 1980 Taylor-Görtler instability of incompressible boundary layers with heat transfer. *Rep. Inst. High Speed Mech.* **42**, Tōhoku Univ.
- [16] KOHAMA, Y. 1984 Study on boundary layer transition of a rotating disk. *Acta Mechanica*, **50**, 193–199
- [17] KOHAMA, Y. & OHTA, F. 1994 Humidity enclosure process enhanced by streamwise vortices developing over the sea. *Exp. Thermal Fluid Science*, **8**, 230–238
- [18] LINGWOOD, R. J. 1995 Absolute instability of the boundary layer on a rotating disk. *J. Fluid Mech.* **299**, 17–33
- [19] LINGWOOD, R. J. 1996 An experimental study of absolute instability of the rotating-disk boundary-layer flow. *J. Fluid Mech.* **314**, 373–405
- [20] LINGWOOD, R. J. 1997a Absolute instability of the Ekman layer and other relating flows. *J. Fluid Mech.* **331**, 405–428
- [21] LINGWOOD, R. J. 1997b On the effects of suction and injection on the absolute instability of the rotating-disk boundary layer. *Phys. Fluids*, **9**, 1317–1328
- [22] MABUCHI, I., TANAKA, T. & SAKAKIBARA, Y. 1971 Studies on the convective heat transfer from a rotating disk. *Bull. JSME*, **14**, 581–589
- [23] MALIK, M. R. 1986 The neutral curve for stationary disturbances in rotating-disk flow. *J. Fluid Mech.* **164**, 275–287
- [24] MATSUBARA, M. & ALFREDSSON, P. H. 1996 Experimental study of heat and momentum transfer in rotating channel flow. *Phys. Fluids*, **8**, 2964–2973
- [25] MILLSAPS, K. & POHLHAUSEN, K. 1952 Heat transfer by laminar flow from a rotating plate. *J. Aeronautical Sciences*, Feb. 1952, 120–126
- [26] NORDLING, C. & ÖSTERMAN, J. 1996 Physics Handbok. *Studentlitteratur*, Lund
- [27] NORTHROP, A. & OWEN, J. M. 1988 Heat transfer measurements in rotating-disc systems Part 1: The free disk. *Int. J. Heat and Fluid Flow*, **9**, 19–26
- [28] POPIEL, Cz. O. & BOGUSLAWSKI, L. 1975 Local heat-transfer coefficients on the rotating disk in still air. *Int. J. Heat Mass Transfer*, **18**, 167–170
- [29] RAHMAN M. M. & FAHGRI, A. 1992 Numerical simulation of fluid flow and heat transfer in a thin liquid film over a rotating disk. *Int. J. Heat Mass Transfer*, **35**, 1441–1453
- [30] RICHARDSON, P. D. & SAUNDERS, O. A. 1963 Studies of flow and heat transfer associated with a rotating disk. *J. Mech. Eng. Science*, **5**, 336–342

- [31] SEDDOUGUI, S. O. & BASSOM A. P. 1996 The effects of suction on the non-linear stability of a three-dimensional compressible boundary layer. *IMA J. Appl. Math.* **56**, 183–206
- [32] SREENIVASAN, K. S. 1973 Laminar mixed convection from a horizontal rotating disk. *Int. J. Heat Mass Transfer*, **16**, 1489–1492
- [33] THEODORSEN, T. & REGIER, A. 1948 Experiments on drag of revolving disks, cylinders and streamline rods at high speeds. *NACA Report 793*
- [34] WANG, C. Y. 1990 Boundary layers on rotating cones, discs and axisymmetric surfaces with a concentrated heat source. *Acta Mechanica*, **81**, 245–251
- [35] WALL, D. P., & WILSON, S. K. 1997 The linear stability of flat-plate boundary-layer flow of fluid with temperature-dependent viscosity. *Phys. Fluids*, **9**, 2885–2898
- [36] WILKINSON, S. P., & MALIK, M. R. 1985 Stability experiments in the flow over a rotating disk. *AIAA Journal*, **23**, 588–595